RESEARCH ARTICLE

Fabrics, facies, and flow through a large-volume ignimbrite: Pampa De Oxaya, Chile

E. S. Platzman[1] · R. S. J. Sparks[2] · F. J. Cooper[2]

Abstract

The Miocene Oxaya Formation, exposed along the western Andean slope in northern Chile, represents one of the largest ignimbrite provinces on earth. In this study, magnetic fabric data were acquired from a ~ 1-km-long core drilled vertically through a single cooling unit of the Oxaya Formation the ca.22 Ma Cardones ignimbrite. Samples for magnetic analysis were obtained every 20 m from the fine-grained matrix of the core. Detailed measurements of the variation in bulk magnetic properties, including natural remanent magnetization (NRM), susceptibility, and anisotropy of magnetic susceptibility (AMS), were used to monitor changes in magnetic mineralogy as well as changes in the strength and orientation of the magnetic fabric throughout the flow. AMS ellipsoid orientation and shape reflect rapid deposition from a concentrated granular fluidized flow and constrain both the location of the source caldera for this catastrophic eruption and processes of transport and deposition in this large-volume ignimbrite. After utilizing the magnetic remanence to correct for rotation about the core axis, well-grouped and imbricated petrofabric orientations reveal a well-defined SW (247°) transport direction down a proto-Western Andean slope indicating syn- or post-welding flow and confirming the deformed Lauca caldera as the likely source of the eruption. Systematic variations in fabric shape (T) and intensity (P) with depth reveal a predominately oblate fabric toward the top and base of the flow and predominately prolate fabrics in the center. These vertical changes in fabric reveal that this massive, apparently homogeneous, deposit has a systematic layering. This layering reflects depth-dependent temperature variations, temporal changes in the flow boundary zone during deposition and post-depositional processes.

Keywords Ignimbrite · Magnetic anisotropy · Mineral fabric · Granular flow

Introduction

The Central Andes of northern Chile and southern Peru exposes the Oxaya Formation, a sequence of four ignimbrites that constitute one of the largest Miocene ignimbrite provinces on Earth (Salas et al. 1966; Wörner et al. 2000; García et al. 2004; van Zalinge et al. 2016). Oxaca Formation ignimbrites form a prominent plateau along the western escarpment of the Western Cordillera (Fig. 1). Ignimbrites of this magnitude (M > 8 using the magnitude scale of Mason et al. 2004) are a result of large catastrophic explosive eruptions and caldera collapse. They commonly travel to distances exceeding 100 km from their source and represent some of the most dangerous and destructive eruptions on the planet. However, because there have been no eruptions of this magnitude in recorded history, fundamental depositional processes within the associated large pyroclastic eruptions remain poorly constrained. Examination of magnetic petrofabrics using the anisotropy of magnetic susceptibility (AMS) can yield important insights into the transport and deposition of these enormous flows as well as post-depositional processes.

Anisotropy of magnetic susceptibility is a technique that measures the strength, orientation, and shape of the rock petrofabric at the centimeter scale as reflected by the shape, distribution, and alignment of its magnetic minerals. Using AMS to delineate the magnetic fabric has been shown to reliably reflect the microscopic rock fabric even in apparently homogeneous rocks (Tarling and Hrouda 1993). Over the last several decades AMS studies of ignimbrites have been used to


✉ E. S. Platzman
platzman@usc.edu

1 Department of Earth Sciences, University of Southern California, 3651 Trousdale Parkway, Los Angeles, CA 9008, USA

2 School of Earth Sciences, University of Bristol, Bristol BS8 1RJ, UK

Fig. 1 Satellite image showing location, with country and provincial boundaries, extent of Oxaya ignimbrites in red (after Brandmeier and Wörner 2016), regional structures, and location of coring site (yellow dot). Inset: map of Andean Cordillera (red), box designates expanded area
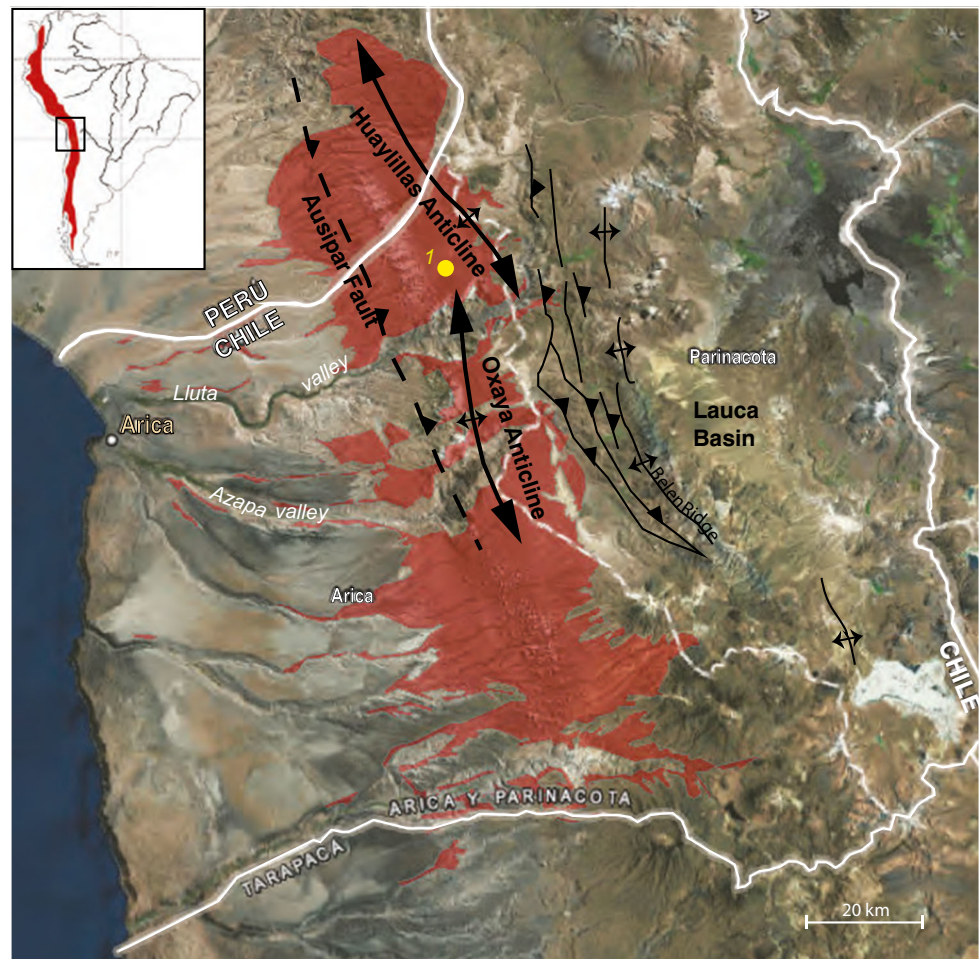
constrain flow patterns and processes in both inter and intra caldera settings. These studies, beginning with Ellwood (1982), are summarized by Cañón-Tapia and Mendoza-Borunda (2014), Willcock et al. (2015), and Ort et al. (2015). Magnetic fabrics in pyroclastic flows have been shown to vary in shape, direction, and intensity with distance from the source caldera and have been used to infer changes in transport direction and depositional process (Fisher et.al. 1993; Baer et al. 1997; Le Pennec et al. 1998; Ort et al. 2003, Porreca et al. 2003, LaBerge et al. 2009; Willcock et al. 2015). Relatively few studies, however, have systematically examined the variation of fabric with depth in a single ignimbrite (MacDonald and Palmer 1990; Hillhouse and Wells 1991; Ort et al. 2003; LaBerge et al. 2009; Willcock et al. 2015).

During a 2012 drilling campaign by BHP along the Western Andean escarpment east of Arica, Chile, nearly 8 km (7773 m) of core was recovered from the early Miocene ignimbrites exposed at or near the surface in 11 holes at elevations ranging from 2336 to 3903 m. The drill cores penetrated through the entire Oxaya formation ignimbrites and into the basement. Samples for this study were collected from a 1.14-km long drill core drilled at an altitude of 3692 m where the Oxaya Formation is exposed at the surface (Fig. 1; Hole 1 in van Zalinge et al. 2016). The core recovered 981 m of ignimbrite and 15 m of underlying sediment and volcaniclastic before penetrating 148 m of basement.

In this study, we use the anisotropy of magnetic susceptibility (AMS) together with microscopy, paleomagnetic, and rock magnetic measurements to characterize the rock fabric in one of the largest members of the Oxaya Formation, the > 1000 km³ Cardones ignimbrite. We present here a petrofabric study of samples collected vertically through ~ 1 km (945 m) of a single cooling unit to evaluate changes in fabric and facies with depth. Our aim is both to place constraints on the location of the source caldera and to investigate depositional processes, emplacement mechanisms, and flow dynamics of this massive eruptive body.

Geologic setting

The Andean margin in northern Chile developed in response to the subduction of the Farallon plate beneath the South

American plate and the resultant formation of a continental magmatic arc (Jordan et al. 1983; Scheuber and Gonzalez 1999; Martinod et al. 2010). In northern Chile, the Andean forarc comprise, from west to east, three major morphological units: the Coastal Cordillera, the Central Depression and the Precordillera or Western Andean Slope. The Coastal Cordillera in the west is composed principally of Mesozoic arc rocks and marine sediments. South of Arica, the Coastal Cordillera is separated from the Tertiary to recent volcanic and sediment of the Western Cordillera and the Altiplano by fanglomerates of the Central Depression. Overlying these fanglomerates and onlapping onto both the Coastal Cordillera at sea level in the west and the present volcanic arc (Western Cordillera) at ca. 4600 m in the east is the Miocene fluvio-volcaniclastic sequence that typifies the Precordillera. This sequence is dominated by a thick succession of large-volume welded ignimbrites of the Oxaya Formation (Salas et al. 1966; Vogel and Vila 1980; García et al. 1996, 2000, 2004; Wörner et al. 2000; Tobar and Salas 2015; van Zalinge et al. 2016).

The Oxaya Formation comprises a sequence of four sub-horizontal, extracaldera ignimbrites. From oldest to youngest these are the Poconchile, Cardones, Molinos, and Oxaya ignimbrites. They are generally thought to have been deposited during a Miocene ignimbrite flare-up related to the acceleration of convergence at the termination of a period of flat slab subduction along this segment of the continental margin (Wörner et al. 2000). The basal flow has been dated at 22.74 ± 0.02 Ma and the uppermost flow at 19.71 ± 0.04 Ma (van Zalinge et al. 2016).

In the study area, the Oxaya Formation defines the modern erosion surface and can be traced 130 km in an E-W direction and 300 km in a N-S direction along the coast of northern Chile and southern Peru (Fig. 1) (Tosdal et al. 1981; Schröder and Wörner 1996; Wörner et al. 2002; García et al. 2004). The total volume of the Oxaya Formation is estimated to be more than 3000 km^3 (Schröder and Wörner 1996).

Since its emplacement in the early Miocene, deformation of the ignimbrite succession in the Pre-Cordillera region has been minor (van Zalinge et al. 2016, 2017a). In the study area, the ignimbrites are gently folded into a series of long wavelength, doubly plunging, asymmetric, en-echelon antiforms, the Oxaya, and Huaylillas anticlines (Fig. 1). The trend of these antiforms varies along their 50 km strike from N-S to 140°. The northernmost Oxaya anticline is bounded on its western limb by the steeply dipping Ausipar fault (van Zalinge et al. 2016), which does not rupture the modern erosion surface but is exposed in the deeply incised Azapa and Luta quebradas (Fig. 1). The drill site is located on the western flank of the Huaylillas anticline. At this location, the Oxaya succession is gently folded and dips ~ 5.7°W. van Zalinge et al. (2016) estimate that approximately 1.2° of this westward

dip reflects the initial dip of the surface at the time of emplacement of the ignimbrites.

The source of Oxaya Formation ignimbrites is not well established. Garcia et al. (2000) suggested that they may have originated from the subsequently deformed Lauca Caldera. The 50×23 km^2 Lauca Caldera occupies a large part of the Cordon Belen and Lauca river basin yet only its western margin is visible (Fig. 1).

Cardones ignimbrite

The Oxaya Formation forms a plateau comprising three distinct large-volume ignimbrites, the Cardones, Molinos, and Oxaya, which overlie the much smaller-volume Poconchile ignimbrite. The large-volume Cardones ignimbrite is exposed over an area of ~ 4200 km^2. Its varies from circa 1 km in the deeply-incised paleo-canyons in the more eastern reaches, to around 100 m on topographic highs and in the more distal western reaches (van Zalinge et al. 2016, 2017a). Minimum volume estimates are on the order of 1260 km^3 (García et al. 2004). The Cardones has a weighted mean ^{238}U/^{206}Pb age of 21.92 ± 0.02 Ma (van Zalinge et al. 2016).

At the coring site, the Cardones ignimbrite is a massive, ~ 1 km thick, eutaxitic, crystal-rich, lithic-poor, and red rhyolitic tuff (Fig. 2). It is ubiquitously welded with pervasively flattened juvenile clasts (fiamme) that are altered to clays at the top and base of the flow. The three main components of the ignimbrite at this location are free crystals, juvenile clasts, and lithic clasts. Free crystal fragments include quartz, plagioclase, potassium feldspar, biotite, and amphibole (Fig. 3a,b) with accessory minerals including magnetite, ilmenite, and hematite. Modal abundance of the crystal fragments varies between 23 and 51% (van Zalinge et al. 2016) and sizes range from < 0.5 to 5 mm. Juvenile clasts constitute < 5% of the bulk ignimbrite and are generally deformed into fiamme. Lithic clasts, more abundant toward the base of the flow, are typically sub-rounded volcanic lapilli of variable composition. The microcrystalline ash matrix is largely devitrified. Based on detailed analysis of clast distribution, welding intensity, and crystal modes, van Zalinge et al. (2016) divided the Cardones ignimbrite into two eruptive units, the lower of which was further divided into four subunits.

Depositional fabrics within the Cardones are defined macroscopically by the orientation of fiamme and the preferred orientation of crystal fragments such as biotite. An almost pervasive imbricated fabric of fiamme and biotite crystals (Fig. 2) is observed at nearly all levels in the flow. Primary welding is evidenced by the presence of devitrified remnant fluidal juvenile shard textures (Fig. 3c), the ubiquitous flattened juvenile fiamme and loading induced, in situ secondary crystal fragmentation (van Zalinge et al. 2018). The observed architecture is likely to arise from numerous factors relating to
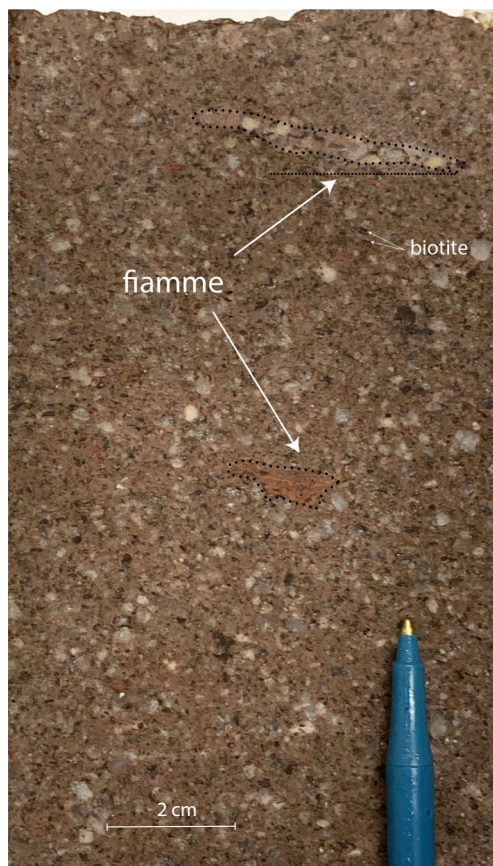
Fig. 2 Hand sample from 260 m showing characteristic eutaxitic texture, mineralogy, and macroscopic fabric of Cardones ignimbrite. Dashed lines delimit imbricated fiamme (fine dotted line is horizontal)

the generation, transport, emplacement and post-emplacement modification of the ignimbrite.

Methods

To avoid overloading the cryogenic magnetometer during rock magnetic analysis, small, ~ 1 cm^3 core samples, were obtained every 20 m primarily from the fine-grained matrix of the drill core. Prior to analysis, samples were weighed and measured to obtain a density profile through the ignimbrite.

Detailed measurements of the variation in bulk magnetic properties including magnetic susceptibility, natural remanent magnetization (NRM) and anisotropy of magnetic susceptibility (AMS) were used to monitor variation in petrofabric intensity, shape, and orientation with depth in the flow. Complementary rock magnetic experiments including isothermal remanence (IRM) acquisition followed by alternating field (AF) demagnetization, low-field magnetic susceptibility vs temperature and thermal demagnetization of 3-component IRM experiments were run on selected samples to characterize the magnetic carriers. Further observations were made using both reflected and transmitted light on an optical microscope.

Low-field AMS was measured on a KLY-3 Kappabridge housed at the University of Southern California. Data analysis was done using Anisoft 4.2 software (Chadima and Jelínek 2008) and Cureval software (Chadima and Hrouda 2009). AMS exploits magnetic susceptibility anisotropy of minerals (see reviews in Martín-Hernández et al. 2004). In an individual mineral crystal, the ability to acquire a magnetization in a specified direction is commonly dependent on crystallography or shape. The magnetic anisotropy of the bulk rock will then depend on its mineralogy, the preferred orientation of the magnetic minerals as well as on the distribution of the magnetic grains within the rock. Closely spaced, strong magnetic grains will interact magnetically and influence the bulk AMS (Hargraves et al. 1991). AMS is commonly expressed as a second rank tensor and represented as an ellipse with principal directions: k_1 maximum, k_2 intermediate, and k_3 minimum ($k_1 > k_2 > k_3$). The mean susceptibility k_{mean} is simply ($k_1 + k_2 + k_3$)/3. By analogy to the strain tensor, the magnetic lineation ($L = k_1/k_2$) is defined as a vector in the direction of k_1. The magnetic foliation ($F = k_2/k_3$) has a direction defined by the pole to the foliation, k_3. The ratio k_1/k_3 (P) thus expresses the degree of anisotropy, which reflects the strength of the magnetic fabric.

The shape of the susceptibility ellipsoid can be represented by a parameter (T) where $T = (\ln F - \ln L) / (\ln F + \ln L)$ (Jelinek 1981). If $k_1 = k_2 > k_3$, the ellipsoid will be flattened (oblate) and T will have a value between 0 and 1 whereas if $k_1 > k_2 = k_3$ it will be elongate (prolate) and T will have a value between 0 and − 1.

As analogous to granular flow in sedimentary systems, the long axis of the susceptibility ellipsoid (k_1) is commonly imbricated parallel to the main flow direction and the pole to the magnetic foliation (k_3) deviates at a small angle (typically < 20°) from the bounding upper surface of the ignimbrite. In some high-concentration flows in which rolling or saltation become important, k_1, like other elongate grains, could align perpendicular to the flow (Ort 1993). Therefore, in this study, analysis of k_3 imbrication was used preferentially to determine the direction of flow.

Results

Density profile

The density profile of an ignimbrite reflects the degree of compaction (Smith 1960; Ragan and Sheridan 1972; Sheridan and Ragan 1975; Sparks et al. 1999; Sheridan and Wang 2005), which is in turn related to its history of temperature, fluid solubility, pressure, loss of porosity and strain. A profile of density vs depth can therefore be used to place constraints on the welding history of the flow (Sheridan and Wang 2005). The large-volume Cardones ignimbrite has a simple density profile exhibiting no obvious breaks or

Fig. 3 Photomicrographs illustrating representative mineralogy (amphibole, amph; magnetite, mt; biotite, bt; plagioclase, plag; quartz, qtz) and textures of Cardones ignimbrite: **a** plane polarized light (ppl) image showing spherules (sph) growing in glass; **b** image under cross polars (xpl) showing embayed quartz (qtz) and fragmented rotated crystals; **c** ppl image displaying devitrified fluidal shards; **d** reflected light image showing opaque minerals, principally iron oxides (Fe-ox), in altered biotite (bt); **e** ppl image showing undeformed glass shard and aligned biotite crystals near unwelded base of ignimbrite (940 m); **f** reflected light image of free titanomagnetite (mt) crystal showing oxyexsolution texture
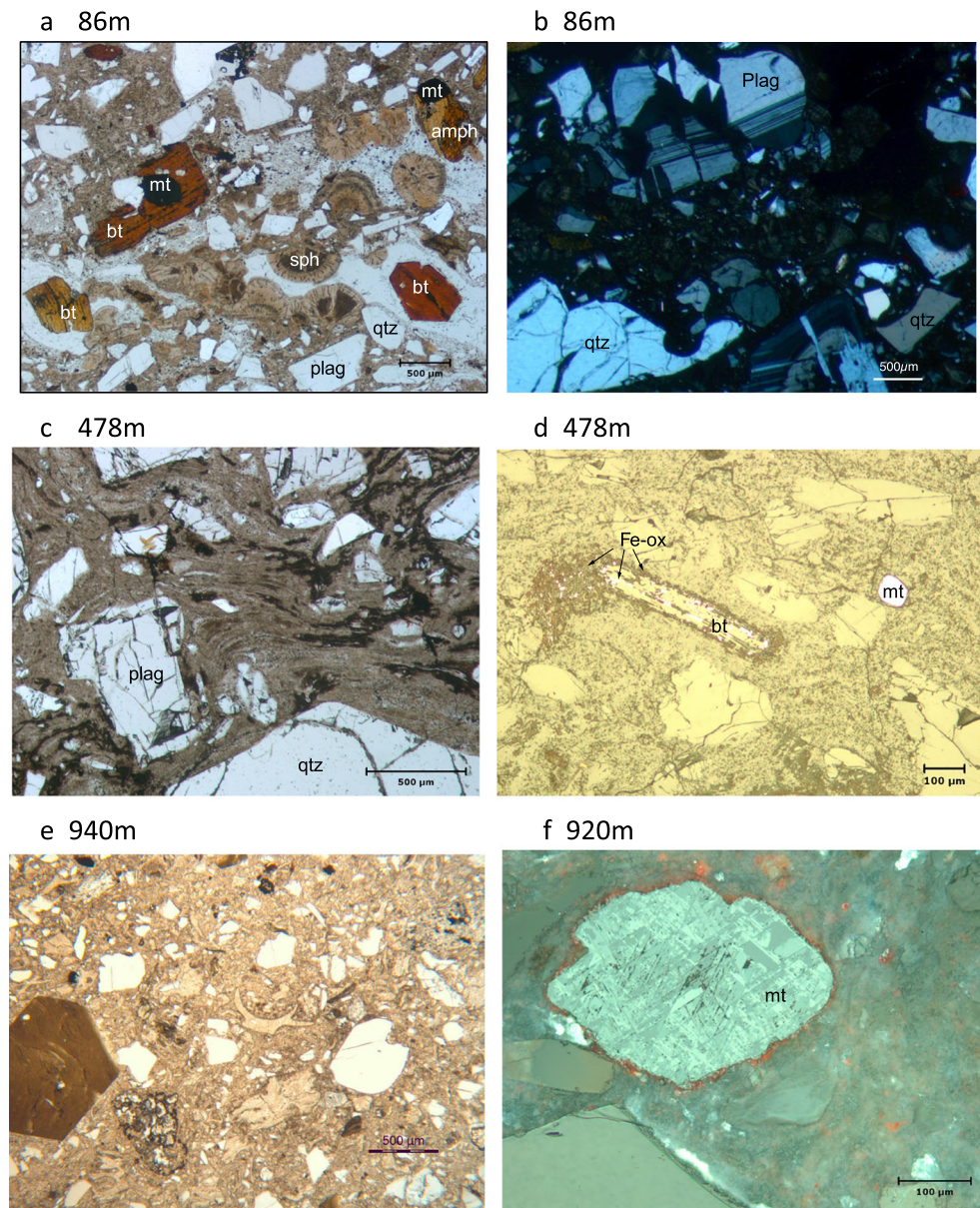
discontinuities (Fig. 4: and van Zalinge et al. 2016, Fig. 6). The density profile divides the ignimbrite into three distinct zones similarly observed in other ignimbrites (Ragan and Sheridan 1972). The upper zone comprises the top 80 m of the flow and shows a rapid linear increase in density with depth from a low of 1900 to a high of 2200 kg/m^3. Although the Cardones is exposed at the surface at the drill site, the first 30 m of the ignimbrite proved to be extremely friable and was not systematically recovered in the drill core. Observations from the other drill cores (van Zalinge et al. 2016), however, indicates that this upper zone can reach thicknesses of > 100 m, indicating that the topmost layer was partially eroded at this location.

Extending from 80 to 880 m depth, excluding outliers that likely include fragments of lower density crystal-rich pumice (van Zelinge et al. 2016), the matrix density increases gradually with depth from 2200 kg/m^3 at 80 m to a maximum value of 2360 kg/m^3 at 880 m. A marked decrease in density is observed 65 m above the base of the flow, at ~ 90% of the total depth and the fiamme aspect ratio decreases markedly below 800 m (van Zalinge et al. 2018). The region of maximum density and pumice deformation is inferred to be where the combined effects of temperature, loading, and volatile dissolution (Sparks et al. 1999) were maximized and where nearly all pore space has been eliminated in the devitrified ignimbrite. The smooth pattern of density variation with depth indicates that, at this location, we are looking at a simple, single cooling unit. The cooling unit may represent a single flow or it could be a composite of many flows that have been emplaced in such rapid succession that they cannot be differentiated (Smith 1960).
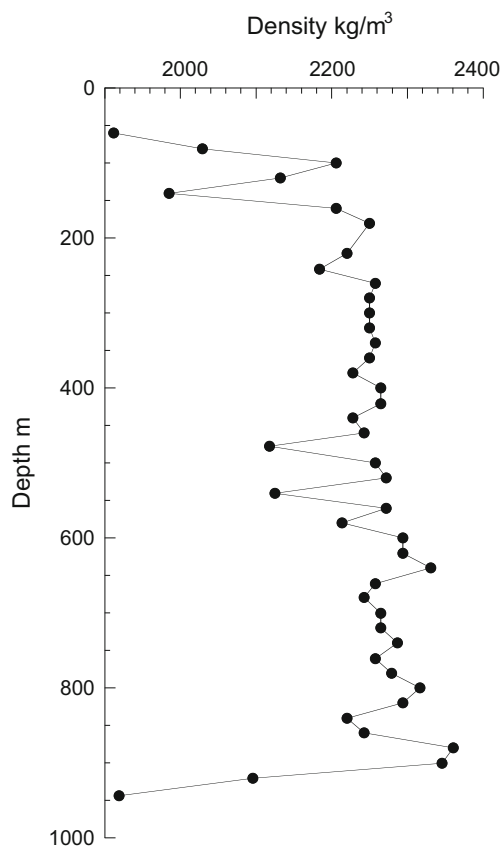
Fig. 4 Plot of bulk density of Cardones samples vs. depth (meters)

Below 880 m, the density of the ignimbrite falls back to a value of 1900 kg/m³, measured close to the base of the flow at 945 m (Fig. 4). Low density at the base of the flow suggests rapid cooling resulting in decreased welding, increased alteration and secondary clay formation.

Microscopy

Iron oxide crystals observable in thin section, represent slightly less then 1% of the total crystal assemblage of the Cardones ignimbrite (van Zalinge et al. 2016, 2017b). This visible iron-oxide assemblage can be further subdivided into four distinct populations.

The first population comprises large, commonly > 100 μm and up to 500 μm, euhedral oxide crystals (Fig. 3f). At all levels in the ignimbrite, most of these large crystals exhibit classic oxidative exsolution (oxyexsolution) textures. Oxyexsolution trellis textures in magnetite and ilmenite or Ti-magnetite are indicative of slow cooling and/or oxidizing conditions. Previous studies have interpreted them as reflecting either a slow ascent of magma prior to eruption (Saito et al. 2004; Turner et al. 2008) or the slow cooling of the ignimbrite after hot emplacement (Bowles et al. 2013; Jackson and Bowles 2014).

The second population of iron-oxides has a very fine, micron to submicron grain-size. This population is barely discernable with the optical microscope yet is prevalent throughout the devitrified groundmass. Previous studies have shown that these ultra-fine oxides can occur both as a primary phase in the ash and as a secondary phase that forms along shard rims and within vesicle walls of pumice fragments during high-temperature crystallization (Schlinger et al. 1988; Thomas et al. 1992; Palmer et al. 1996; Pioli et al. 2008).

A third group of iron oxides consists of those associated with primary inclusions in, or secondary alteration of, biotite and amphibole. Primary inclusions as shown in Fig. 3a tend to occur as large inclusions (tens of μm) while iron oxides resulting from alteration and mineralization (Fig. 3d) typically have grain sizes < 10 μm. They are commonly concentrated along cleavage planes or surrounding the altered biotite and amphibole reaction rims (van Zalinge et al. 2017b) or overgrowths. Tabular, euhedral biotite (2–4 vol%) is widespread throughout the ignimbrite with crystals typically ~ 100 μm in width. The extent of alteration and the amount of magnetite/hematite inclusions, however, are observed to vary markedly with depth in the ignimbrite. The less-dense top and bottom zones of the ignimbrite have fewer and predominately unaltered biotite crystals (Fig. 3a,e). The high-density, intensely welded, central section of the flow, in contrast, has abundant iron oxides associated with increased alteration and deformation of the biotite. Therefore, although biotite abundance, size, and shape-preferred orientation contribute to the magnetic susceptibility throughout the ignimbrite, at depths where biotite alteration and magnetite exsolution is prevalent, alteration products are likely to dominate the anisotropy of magnetic susceptibility.

The final population of iron oxides is associated with the lithic inclusions. Volcanic fragments, predominately of andesitic and granitic composition, typically contain primary iron oxides of magmatic origin.

Paleomagnetic results

Characteristic remanent magnetization

Initial measurements of natural remanent magnetization (NRM) measured on a 2G magnetometer in the Paleomagnetism Laboratory at Occidental College reveal a variation with depth in the flow reflecting changes in both the concentration and the mineralogy of the remanence-carrying fraction (Fig. 5a). The NRM profile further subdivides the flow into four distinct units that broadly correspond with the subunits defined by van Zalinge et al. (2016) based on juvenile and lithic clast distribution. The uppermost unit, defined by the top ~ 190 m of the core, reveals NRM intensities that vary about a mean value of 0.45 A/m. Below this layer, at depths of ~ 190–650 m, we observe a distinctive

Fig. 5 Natural remanent magnetization (NRM) of the Cardones ignimbrite. **a** Plot of NRM vs depth; **b** Vector diagram of alternating field (AF) demagnetization of NRM of sample FCD1435. Each division on axis is 1×10^{-5} emu. The squares represent the tip of the paleomagnetic remanence vector at a specific AF demagnetization level. The blue/yellow squares represent the projection of the vector on the horizontal (Decl.) and vertical (Incl.) planes respectively. Inset shows normalized remanent magnetization (J/J_{max}) as a function of demagnetizing field
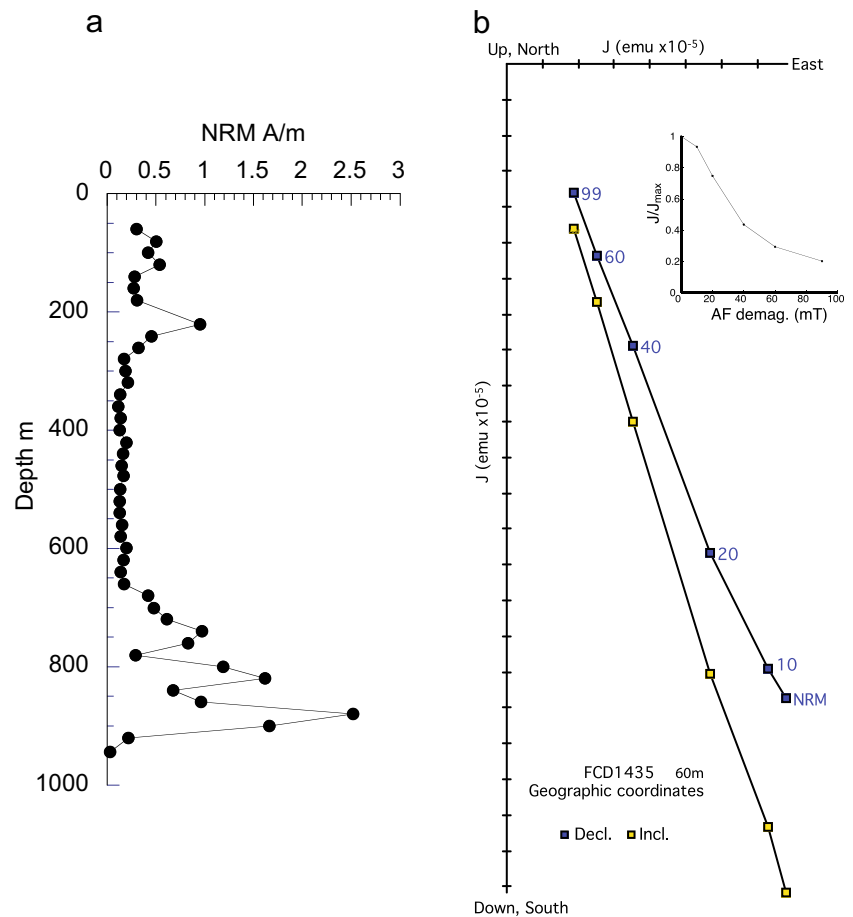
interval characterized by anomalously low NRM intensities (0.15 A/m) with little variability (± 0.03). In contrast, the third zone at depths of ~ 650–900 m, displays higher magnetization intensities and high variability. NRM intensities in this lower unit are observed to increase stepwise to reach a maximum value of 2.52 A/m at a depth of 900 m. This increase in intensity and variability likely reflects an increase in andesite and granite lithic content (van Zalinge et al. 2016). Below 900 m, within the low-density unit at the base of the ignimbrite, NRM intensities decrease precipitously by two orders of magnitude from 2.52 to 0.03 A/m.

NRM was routinely demagnetized in alternating magnetic fields (AF) of 10, 20, 40, 60, and 90 mT. A typical plot of intensity loss as a function of AF demagnetization is shown in Fig. 5b. In most samples, half of the initial remanent intensity is lost by ~ 30–35 mT and typically $\sim 80\%$ is lost by 90 mT. These experiments reveal that the NRM is composed of one or, in some cases, two overlapping components of remanent magnetization. The characteristic remanent magnetization (ChRM) demagnetizes straight toward the origin of demagnetization plots. ChRMs were generally determined from 4 to 5 demagnetization steps from 10/20 mT to 90 mT with an average maximum angular deviation (MAD) of 2.8°. The broad

coercivity spectrum observed reflects a range of magnetic grain sizes and mineralogy.

In a large-volume welded ignimbrite, the direction of the magnetic remanence vector will typically record the direction of the Earth's magnetic field either at the time the flow cooled through the Curie temperature of the constituent magnetic minerals or at the time the magnetic assemblage grew through the blocking volume. Substantial welding (Dingwell 1998; Russell and Quane 2005) indicates emplacement temperatures above the Curie temperature of magnetite (575 °C) and the resulting remanence of the primary mineral assemblage is likely to be thermal in origin (thermal remanent magnetism; TRM). The predicted declination and inclination for the axial-dipole at this latitude are 359° and − 34°. Individual measured declinations, however, scatter randomly within the plane normal to the core axis ($\alpha_{95} = 90$) because of the inherent degree of freedom of rotation about the axis of the drill core. In contrast, observed inclinations have a mean value of $37° \pm 12°$ ranging from 12 to 68° with a generally Fisherian distribution. Statistical analysis of inclination-only paleomagnetic data (McFadden and Reid 1982; Enkin and Watson 1996; Arason and Levi 2010) demonstrates that the inclination measured in a drill core will, on average, be shallower than the true average

inclination with the amount of apparent flattening dependent on the magnitude of the inclination. For an average inclination of 37°, apparent flattening is predicted to be less than 1° (Arason and Levi 2010). The magnitude of the average inclination is not significantly different from the predicted value of 34° for the axial-dipole at this latitude. The polarity, however, is consistently reversed, indicating that the Cardones ignimbrite was emplaced and acquired a TRM or thermochemical remanent magnetism (TCRM) during a single reverse polarity interval. Constraints from U/Pb geochronology (21.92 ± 0.02 Ma 2 σ; van Zalinge et al. 2016) indicate that the Cardones ignimbrite was erupted during chron 6AAr (21.877–22.166 Ma) of the magnetic polarity time scale (MPTS) of Cande and Kent (1995).

Rock magnetic results

Measurement of bulk magnetic susceptibility and magnetic susceptibility vs temperature shows that the mean susceptibility of the Cardones ignimbrite is 31.97×10^{-4} SI ranging from $4.95–58.08 \times 10^{-4}$ SI. The susceptibility versus depth profile largely mirrors the density profile (Fig. 6a), increasing gradually with depth before falling off precipitously toward the base of the flow. A simple biplot of density vs susceptibility shows a good correlation ($R = 0.78$). (Fig. 6b). This correlation suggests that, as the density and welding intensity increases, the concentration of magnetic minerals also increases.

Bulk low-field magnetic susceptibility vs temperature was measured on samples from five depths: 30 m, 80 m, 478 m, 920 m, and 944 m. Figure 7 displays three characteristic curves. Results indicate only minor variations in magnetic mineralogy with depth. In most of the samples, heating and cooling curves are similar, indicating that the susceptibility is reversible and new magnetic material was not created during the experiments. Throughout much of the flow, the dominant carrier appears to be magnetite with a Curie temperature approaching 575 °C (525–580 °C). However, in most samples, additional magnetic phases including titanomagnetite, maghemite, and hematite, are also evident. At 478 m (sample FCD1456, Fig. 7b), we observe a marked increase in susceptibility resulting from heating that may reflect an increased contribution of paramagnetic phases such as biotite, which is more conspicuous in thin section at intermediate depths. Samples FCD1478 and FCD1479 (920 and 944 m) collected near the base of the flow display Curie temperatures above 600 °C, more indicative of hematite, and heating curves with multiple inflection points, suggestive of several magnetic phases (Fig. 7c).

Isothermal remanent magnetization (IRM) acquisition curves indicate a dominance of low coercivity magnetic minerals that begin to saturate in fields of ~ 0.1 T but rarely completely saturate, even at the maximum field of 1 T. The magnetized samples were subsequently stepwise AF demagnetized and the IRM acquisition versus demagnetization
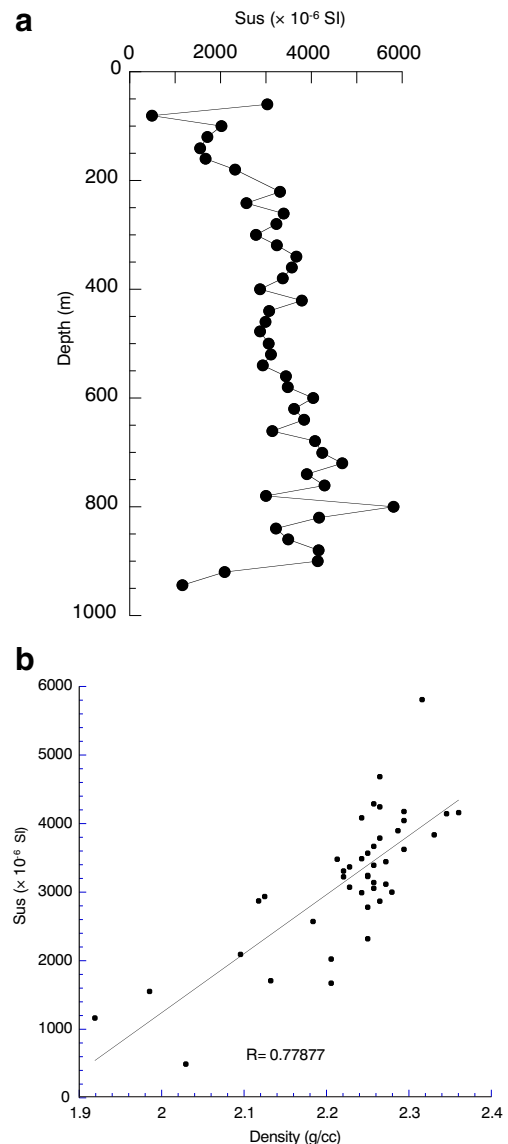
Fig. 6 a Plot showing variation of magnetic susceptibility (Sus) through the 1 km simple flow unit. **b** Plot of density vs magnetic susceptibility. R is correlation coefficient

is shown in Fig. 8a. Results show the intersection of the magnetization and demagnetization curves, at fields approximating the coercive force (Hcr), and yield "R" values (ratio of the saturation remanence demagnetized to the coercive force to the undemagnetized saturation remanence), consistently < 0.40 and, in some cases, as low as 0.27, indicating a prevalence of strongly interacting magnetic particles (Cisowski 1981). The acquired IRM is almost completely erased in AC fields of only 100 mT also pointing to strong interaction fields. A complementary experiment (Fig. 8b) comparing the AF demagnetization behavior of IRM and anhysteretic remanent magnetization (ARM) known as the Lowrie-Fuller test (Lowrie and Fuller 1971; Johnson et al. 1975) indicates that the stable remanent magnetization is likely to be held predominantly in a small (~ 0.05 to ~ 10 μm), single domain (SD), or pseudo-single domain
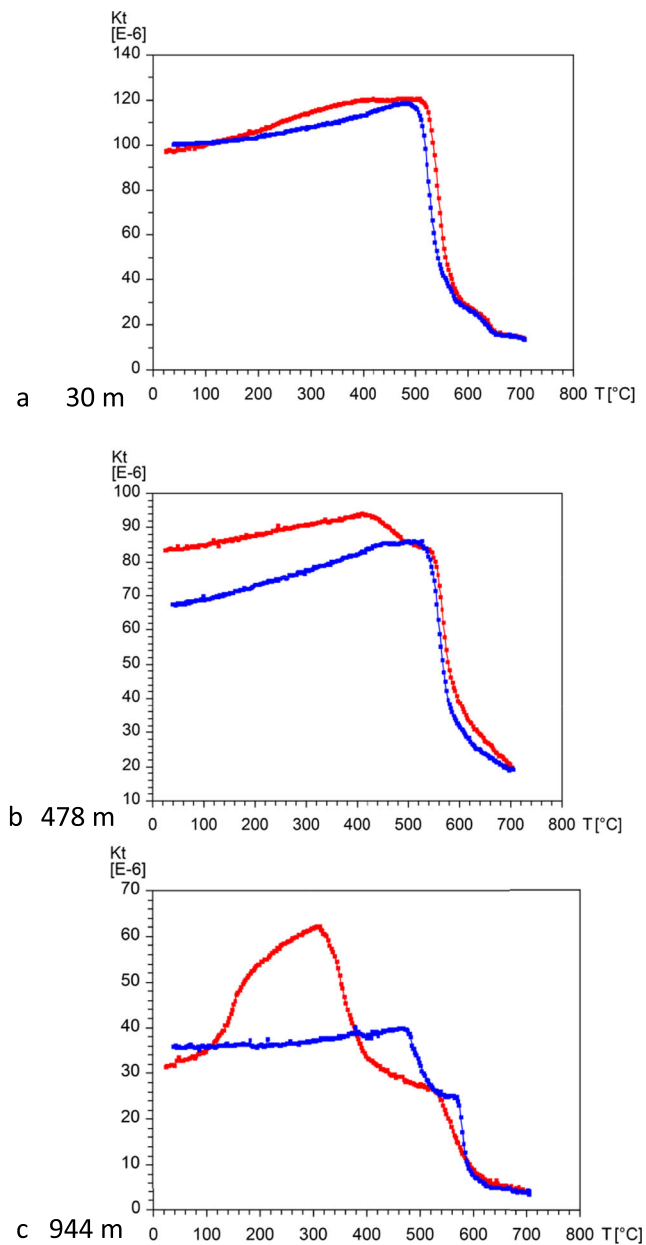
Fig. 7 Temperature dependence of low-field magnetic susceptibility (Kt × 10^{-6}); heating in red and cooling in blue, for three depths (30 m, 478 m, 940 m) showing evidence of magnetite, hematite, and clay

Fig. 8 **a** IRM acquisition vs. saturation remanence (SIRM) AF demagnetization experiments. The intersection of the two curves at $R < 0.4$ (normalized remanent magnetization, J/J$_{max}$) indicates closely packed weakly interacting magnetite (Cisowski 1981). **b** the Lowrie-Fuller test (Lowrie and Fuller 1971) using results from anhysteretic remanent magnetization (ARM) and isothermal remanent magnetization (IRM) experiments. The tests indicate small magnetic particle size (single domain or pseudosingle domain size)

(PSD) particles. Mean destructive fields (MDF), typically < 40 mT corroborate this.

In a final rock magnetic experiment (Fig. 9), samples were given three components of IRM magnetization in fields of 0.12 T, 0.3 T, and 1.0 T sequentially along the x, y, and z axis of the sample. The samples were then stepwise thermally demagnetized. This procedure characterizes the magnetic carriers based on both their coercivity spectrum and their unblocking temperature characteristics (Lowrie 1990). Results reveal that the magnetization is held principally in the low coercivity fraction, which demagnetizes between 575 and 625 °C. This confirms that the principal carrier of
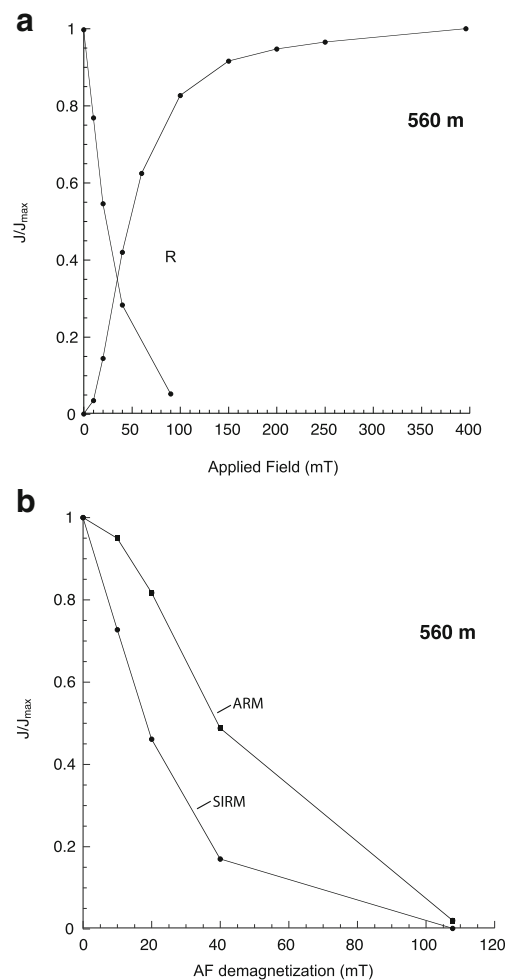
the remanent magnetization is likely to be interacting magnetite particles. The remaining smaller portion of remanent magnetization resides in the highest coercivity fraction, which demagnetizes at 675 °C, characteristic of hematite.

AMS results

The AMS tensor has a magnitude, represented by anisotropy parameter P, a shape represented by anisotropy parameter T, and a spatial orientation (Table 1).

The anisotropy parameter P (k$_1$/k$_3$), shown in Fig. 10a as a function of depth in the flow, ranges from 1.015 to 1.099, indicating that the percent magnetic anisotropy varies from ~ 1 to ~ 10%. Higher values of P tend to be recorded between 200 and 550 m depth. There are additional spikes in P deeper in the flow, with the highest value at 944 m. To constrain the
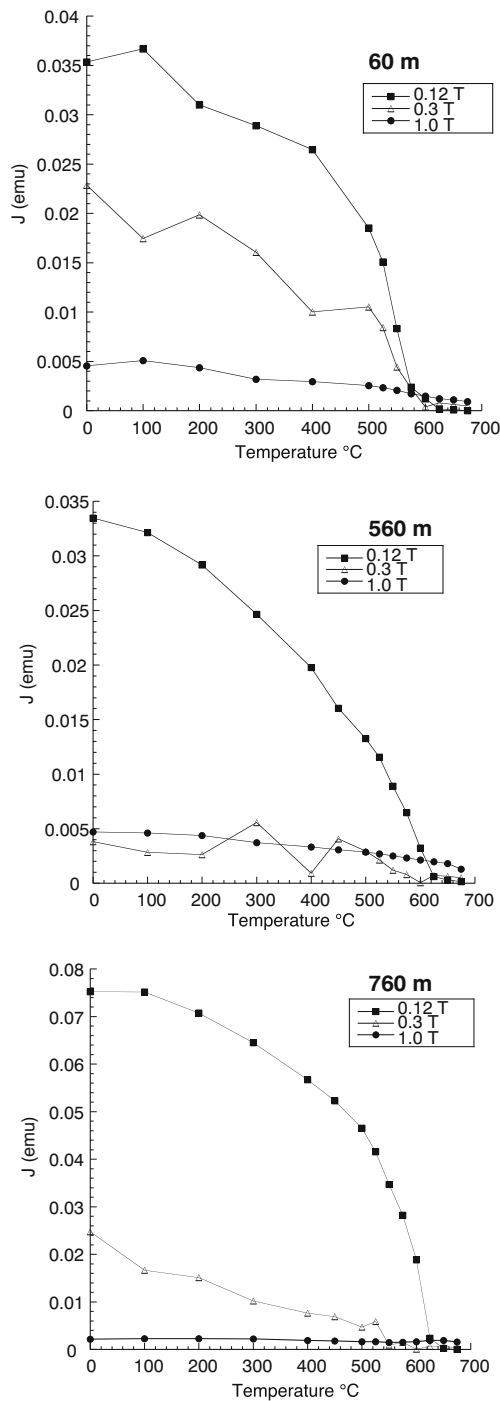
Fig. 9 Stepwise thermal demagnetization of 3-component IRM (Lowrie 1990) for representative samples at increasing depths. Plots show remanent magnetization (J) vs demagnetization temperature of the high (1 T), intermediate (0.3 T) and low-coercivity (0.12 T) components, denoted with circles, triangles, and squares, respectively

origin of this variation, we examine the relationship of P with other rock magnetic parameters. Rheological control (composition, concentration) of fabric intensity would be expected to

Table 1 Anisotropy of magnetic susceptibility data for the Cardones ignimbrite

Sample	Depth (m)	$K_{mean} \times 10^{-6}$ SI	L	F	P	T
1435	60.08	3029.4	1.008	1.019	1.027	0.425
1436	81.22	494.89	1.006	1.017	1.022	0.488
1437	100.03	2022.9	1.004	1.022	1.026	0.691
1438	120.08	1708.1	1.009	1.014	1.023	0.221
1439	140.74	1553.5	1.007	1.011	1.018	0.194
1440	160.48	1671.2	1.006	1.009	1.015	0.239
1441	180.45	2322.2	1.017	1.007	1.024	−0.426
1443	220.91	3308.2	1.037	1.027	1.065	−0.155
1444	241.92	2572.8	1.026	1.012	1.038	−0.351
1445	260.7	3390.9	1.006	1.021	1.027	0.547
1446	280.08	3228.7	1.028	1.018	1.046	−0.226
1447	299.94	2781.9	1.016	1.01	1.026	−0.217
1448	319.85	3246.4	1.068	1.013	1.082	−0.665
1449	340.05	3669.7	1.048	1.014	1.062	−0.549
1450	359.94	3569.4	1.033	1.006	1.04	−0.681
1451	379.95	3369.5	1.046	1.011	1.058	−0.599
1452	399.95	2870.6	1.033	1.024	1.057	−0.153
1453	421.19	3787.4	1.041	1.022	1.064	−0.299
1454	440.07	3073.7	1.057	1.01	1.068	−0.698
1455	460.26	2995.2	1.057	1.01	1.067	−0.7
1456	477.93	2871.4	1.044	1.013	1.058	−0.541
1457	500.25	3057.4	1.022	1.027	1.05	0.097
1458	520.18	3116.6	1.025	1.023	1.049	−0.043
1459	540.16	2936.1	1.019	1.012	1.031	−0.236
1460	560.28	3443.5	1.029	1.011	1.04	−0.457
1461	580.05	3481	1.015	1.021	1.036	0.171
1462	599.98	4046.3	1.011	1.013	1.024	0.062
1463	620.21	3624.1	1.01	1.01	1.02	0.012
1464	640.17	3837.4	1.012	1.01	1.022	−0.115
1465	660.9	3140.1	1.034	1.009	1.044	−0.565
1466	679.72	4084.4	1.03	1.029	1.061	−0.017
1467	700.86	4242.6	1.006	1.019	1.025	0.546
1468	720.04	4685.1	1.017	1.014	1.032	−0.102
1469	740.06	3897.8	1.009	1.01	1.02	0.044
1470	760.9	4289.6	1.004	1.019	1.023	0.666
1471	780.53	3001.4	1.018	1.013	1.031	−0.152
1472	800.05	5807.7	1.051	1.015	1.067	−0.533
1473	820.2	4174.5	1.007	1.026	1.033	0.581
1474	840.34	3223.1	1.007	1.011	1.018	0.259
1475	860.07	3487.2	1.009	1.017	1.026	0.337
1476	880.08	4161.3	1.01	1.025	1.035	0.436
1477	900.47	4142.5	1.008	1.043	1.051	0.69
1478	920.4	2093.1	1.013	1.017	1.031	0.123
1479	944.09	1166.7	1.043	1.054	1.099	0.119

$K_{mean} = (k_1 + k_2 + k_3)/3$; L: lineation (k_1/k_2); F: foliation (k_2/k_3); P anisotropy degree (k_1/k_3); T: shape parameter
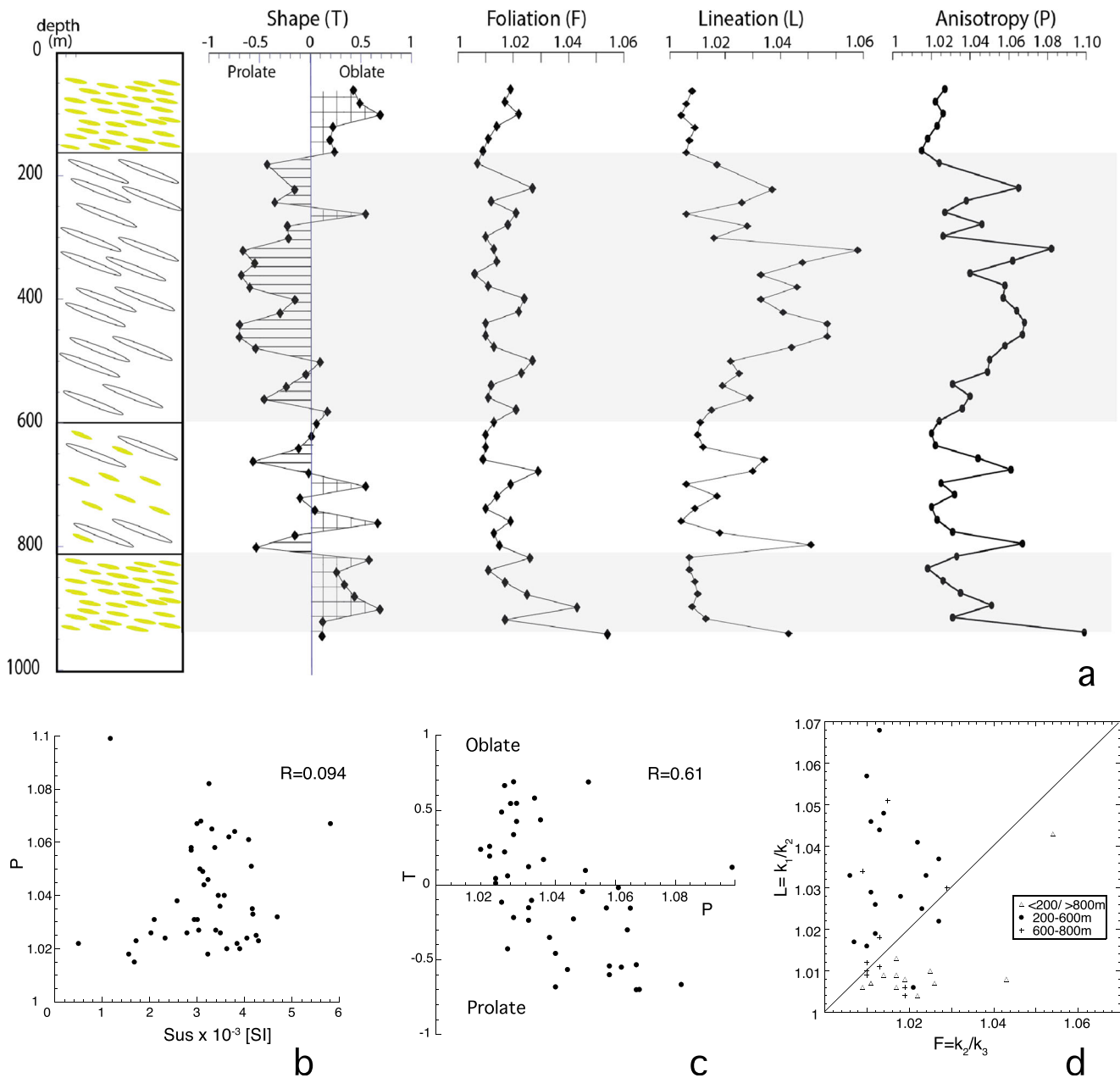
Fig. 10 Magnetic petrofabrics of the Cardones ignimbrite. **a** Schematic stratigraphic column illustrating variation of magnetic fabric, imbrication and shape (yellow/white represent oblate/prolate ellipse) with height in flow. Corresponding variations in magnetic shape parameter (T), magnetic foliation (F), magnetic lineation (L) and magnetic anisotropy parameter (P); **b** anisotropy parameter (P) vs susceptibility (Sus); **c** (T) vs (P); **d** Flinn diagram of AMS ellipsoids with triangle, dot, and cross indicating samples from marginal (< 200/> 800 m), internal (200–600 m), and transitional (600–800 m) depths respectively

lead to a correlation of P with compositional layering. Compositional layering in an ignimbrite can result from changes in clast population supplied at source or temporal changes in physical conditions within the flow. Comparison of the anisotropy parameter P with the magnetic susceptibility (Fig. 10b), a proxy for magnetic mineral concentration, reveals that these parameters are poorly correlated ($R = 0.094$). Likewise, a comparison of P with the NRM intensity, which reflects the concentration of only the remanence-carrying magnetic fraction, shows a poor correlation ($R = 0.13$), indicating that the observed variation in P in the vertical profile is not primarily a function of the composition or concentration of magnetic minerals. This conclusion is corroborated by geochemical analyses that show the Cardones ignimbrite has a largely homogeneous bulk composition and nonsystematic variation in pumice geochemistry (van Zalinge et al. 2016).

It is also possible that the fabric intensity might be principally related to the degree of welding and compaction, which is expected to increase with depth in the flow. Near the base of the flow at 945 m (Fig. 10a), an anomalously high value of P (1.1) implies that there may have been enhanced compaction and shear at this level. In general, however, P is largely uncorrelated with density ($R = 0.04$), leading us to conclude that compaction-welding is not the primary cause of the observed changes in fabric intensity.

In contrast, a comparison of P with the shape parameter T (Fig. 10c) reveals a significant inverse correlation ($R = 0.61$), suggesting that changes in fabric intensity (P) are associated with the changes in fabric shape (T). Lower degrees of anisotropy (P) are largely associated with oblate fabrics and higher degrees of anisotropy with prolate fabrics.

The shape of the AMS ellipsoid, as defined by the T parameter, varies from prolate to oblate with values varying from + 0.691 to − 0.700 (Fig. 10a). As shown on the Flinn diagram in Fig. 10d, oblate, dominantly planar, fabrics are chiefly associated with the uppermost and basal margins of the core while prolate, linear fabrics dominate the central regions. In detail, above a nonerosive, frictional, contact with the substrata, the basal 125 m (820–945 m) shows a well-defined triaxial oblate fabric ($T = 0.364$, $F = 1.028$, $L = 1.014$). In this interval (~Unit 1, subunit 1 of van Zalinge et al. 2016), the magnetic foliation dips 12° to 066° and biotite is well aligned. This layer also shows evidence of inverse grading, with mean grainsize and percentage of free crystals as well as the number of lithic fragments increasing upward (van Zalinge et al. 2016).

The overlying ~ 200 m (600–820 m: ~Unit 1, subunit 2 of van Zalinge et al. 2016), is an interval of inconsistent fabrics. By 820 m, P is at a minimum ($P = 1.01$) and the magnitude of the magnetic foliation has fallen to $F = 1.015$, where it remains, with little change ($\sigma = 0.006$), up to the surface (Fig. 10a). At this depth, the orientation of the foliation has steepened, dipping 19.8° to 254°, indistinguishable from the mean. In contrast, the magnitude of the magnetic lineation (L) becomes remarkably unstable, swinging from $L = 1.004$ to $L = 1.051$. As a consequence, the shape parameter (T) also fluctuates repeatedly from prolate to oblate ($−0.565 < T < + 0.666$) in this interval (Fig. 10a).

At a depth of approximately 600 m, fabric intensity (P) begins to rise, accompanied by a corresponding increase in the magnitude of the magnetic lineation (Fig. 10a). In response, the fabric shape transforms to a triaxial prolate ellipsoid and remains prolate for the next ~ 400 m ($T = −0.296$, $F = 1.015$, $L = 1.032$). It is also in this interval, 180 m–600 m (~Unit 1, subunit 3 of van Zalinge et al. 2016), that the largest fiamme aspect ratio is measured and biotite becomes clearly altered and exsolved (Fig. 3d). Flattened and deformed shards (Fig. 3c) are visible in thin section. Observations of linear magnetic fabrics imply that there is likely to have been an increase in shear strain in this interval.

In the uppermost unit, defined magnetically above 180 m, fabrics once again become oblate (T = 0.376, F = 1.015, L = 1.007). This unit is characterized by a decrease in welding and alteration and the appearance of elongate vesicles (Fig. 3a). It also has a measurably weaker anisotropy ($P = 1.022$). Fragmented crystals (Fig. 3b) and visible void spaces are observed while spherulites (Fig. 3a) indicate crystallization from high temperatures in supercooled melts (Breitkreuz 2013).

The orientation of the AMS tensor is represented in Fig. 11 by an equal area projection of the directions of the principal susceptibility axes of the AMS ellipsoids. As in most layered deposits the orientation of the uncorrected k_3 minimum axes of the anisotropy tensors (Fig. 11a) scatter around the normal to the depositional surface (≈vertical). In contrast, because the core was not oriented during drilling, unconstrained rotation about the drilling axis causes the directions of the maximum and intermediate axes (k_1 & k_2) to scatter randomly within the

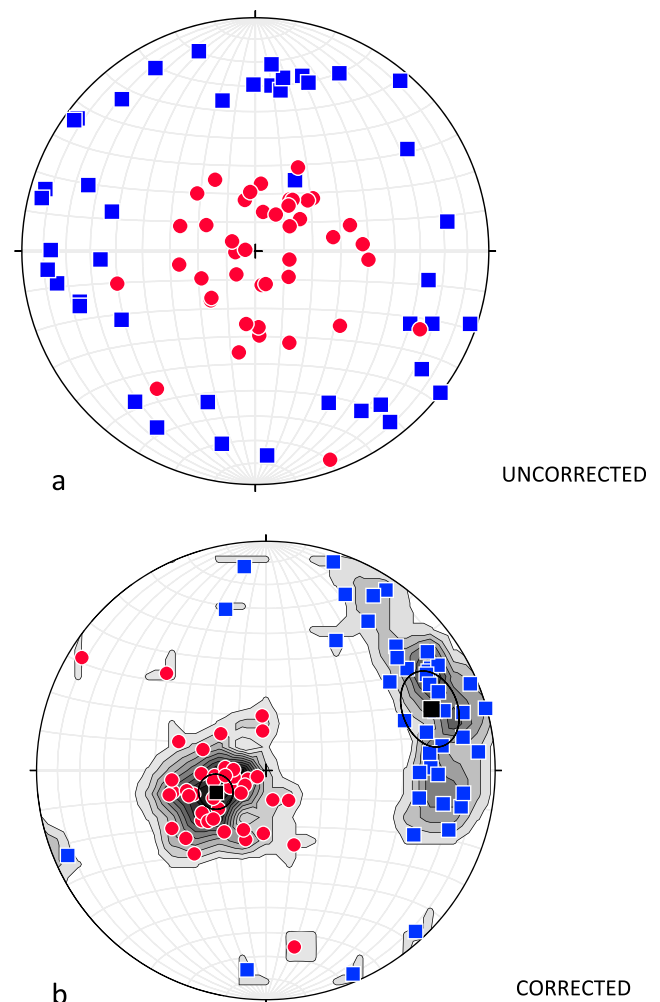a   UNCORRECTED

b   CORRECTED

Fig. 11 Equal area stereographic projection of **a** uncorrected maximum (k_1, blue squares) and minimum (k_3, red circles) susceptibility axes; **b** k_1 and k_3 axes after correction for rotation about the core axis. Contour interval = 2%. Black square shows mean direction with 95% confidence interval

plane normal to the core axis (Fig. 11a) . However, because this late rotation affects both orientation of the remanence vector (NRM) and the AMS tensor, we can use the NRM to correct the orientation of the anisotropy ellipsoid. The NRM of the Cardones ignimbrite was acquired at a time when Earth's ambient magnetic field was reversed, in a direction that was down and toward the south. Rotation about the drill-core axis, which is approximately normal to bedding, should leave the magnetic inclination unchanged. Therefore, simply rotating the declination back to south should, to a first approximation, correct the NRM for the superimposed drilling rotation. The same angular rotation applied to the AMS ellipsoid should, therefore, also correct its orientation for the rotation associated with core recovery. The corrected orientation is expected to vary about the true direction because this correction does not account for variation inherent in the NRM direction due to processes such as secular variation. Uncorrected secular variation, acquired as the flow cooled slowly through the blocking temperature of its magnetic mineral assemblage, would result in increased directional scatter. Despite its limitations, application of this simple correction significantly improves the clustering of the axes of the susceptibility ellipse. Figure 11 shows the orientation of the principal susceptibility axes, k_1 (magnetic lineation) and k_3 (pole to magnetic foliation), before (Fig. 11a) and after (Fig. 11b) this simple correction. Corrected k_3 axes reveal a well grouped mean of 71° toward 247° ($\alpha_{95} = 6.2°$; $K = 13.5$), indicating a well-defined imbrication of the magnetic foliation of 19°. Investigation of imbrication as a function of depth in the ignimbrite suggests that the hot-welded interior shows a somewhat steeper imbrication than the less welded margins. Given, however, that the two populations both have an $\alpha_{95} \sim 6°$, this result is highly suggestive but not statistically significant at the 95% confidence level.

The statistically simple/single flow direction throughout the 1 km thick unit implies that during deposition, as the topography progressively infilled, AMS orientations did not vary appreciably in response to changing boundary conditions, as has been observed in other studies (Hillhouse and Wells 1991; Baer et al. 1997; Branney and Kokelaar 2002; Ort et al. 2003; LaBerge et al. 2009; Cas et al. 2011). This result, together with previously published observations of considerable thickness variations within the Cardones ignimbrite across the Andean forearc (van Zalinge et al. 2016) indicate that the flow at this location was constrained by a deep (~ 1 km) major paleovalley in which the flow developed a well-defined fabric orientation. If the measured SW flow direction (247°) is presumed to have been down the paleoslope away from the source caldera (Ellwood 1982; Incoronato et al. 1983; Knight et al. 1986; MacDonald and Palmer 1990; Hillhouse and Wells 1991; Seaman et al. 1991; Ort 1993; Fisher et al. 1993; Lamarche and Frogatt 1993; Palmer and MacDonald 1999; Ort et al. 2003; Cas et al. 2011; Dedzo et al.

2011), then our result supports the proposed source area of García et al. (2000). They suggested that the Oxaya Formation was the equivalent of the coeval intracaldera Lupica formation farther east, which is exposed and deformed in the Cordon Belen and Lauca river basin (Fig. 12).

Discussion

A pyroclastic flow is a mix of hot gas and particles that emanates from an explosive volcanic eruption. The internal architecture of the resulting ignimbrite reflects the complex interactions and processes occurring at the source, during transport and deposition and post emplacement. Here, we discuss the origin of the magnetic petrofabric and interpret the internal architecture of the Cardones ignimbrite in terms of fabric-forming processes.

Origin of the magnetic petrofabric

Microscopy and rock magnetic experiments show that the Cardones ignimbrite has a magnetic mineral fraction that is a mixture of paramagnetic and "ferromagnetic" (used generally for remanence carrying phases) phases. Paramagnetic minerals including biotite, amphibole, plagioclase, and ilmenite and ferromagnetic minerals, including magnetite and hematite/maghemite occur throughout the flow. Given this mixture, the ferromagnetic mineral phases are predicted to dominate the AMS signal because the intrinsic susceptibility of the paramagnetic phases is orders of magnitude lower than that of the ferromagnetic minerals.

In the Cardones ignimbrite the ferromagnetic Fe-oxides occur as free crystals, inclusions in other minerals (notably biotite and amphibole) and as a component of the devitrified fine grained matrix. Large free crystals of magnetite, which comprise the majority of the free opaque minerals, typically form in a magma before eruption and exsolve sub-micron magnetite and ilmenite lamellae during cooling. These large subhedral Fe-oxide crystals contribute to the bulk magnetization of the ignimbrite. However, because they are largely equant with cubic symmetry and isotropic magnetic properties and are well dispersed within the matrix, these crystals are unlikely to have a significant influence on either the orientation or shape of the AMS tensor. Likewise magnetic minerals incorporated into roughly equant, randomly oriented igneous lithics will contribute to the bulk magnetization but little to the shape or orientation of the anisotropy ellipse.

In contrast with the large, free Fe-oxides crystals, Fe-oxide inclusions in other mineral grains and ultra-fine Fe-oxides within the matrix and along the edges of pumice are likely to make a substantive contribution to the magnitude, shape, and orientation of the magnetic tensor. Fe-oxide inclusions in biotite are observed as both primary magmatic inclusions and
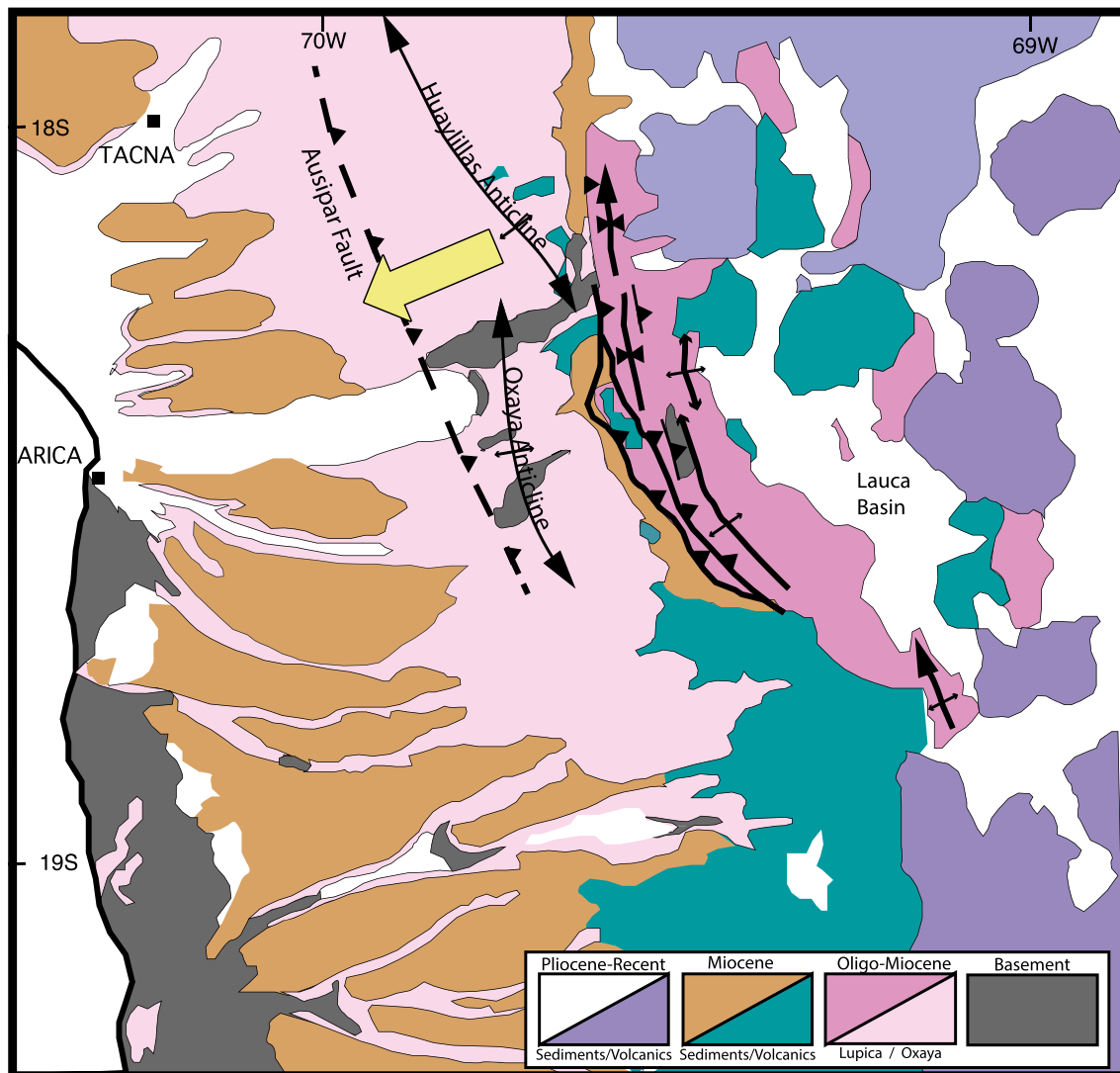
Fig. 12 Simplified geologic map (after Garcia et al. 2011) core location at tail of yellow arrow indicating ignimbrite flow direction

as secondary inclusions formed by subsequent alteration. These two populations vary in concentration with depth in the ignimbrite. Primary magnetite inclusions, which appear commonly as isolated crystals in unaltered biotite and amphibole, are observed predominately at the top (< 200 m) and toward the base (> 600 m) of the flow. At intermediate depths (∼ 200 to 600 m) the biotite is generally altered with the replacement products pseudomorphing the original mica. A consequence of this replacement reaction is the exsolution of magnetite and ilmenite along cleavage planes and as overgrowths along the crystal margin where it is partly oxidized to maghemite or hematite (Fig. 3d). This secondary Fe-oxide growth will contribute to the AMS in this interval and enhance the fabric related to the biotite.

Rock magnetic experiments suggest that the magnetization of the ignimbrite largely originates from interacting single domain (SD) or pseudo-single domain (PSD) magnetite particles. This includes the fine-grained magnetite

observed along biotite cleavage planes in reaction rims but also includes the sub-micron ultrafine magnetite in the matrix and along the edges of pumice. Sub-micron, ultra-fine-grained magnetite has been reported in a number of other high-temperature silicic ignimbrites (Geissman et al. 1983; Schlinger et al. 1988; Wolff et al. 1989; Thomas et al. 1992; Pioli et al. 2008; Worm and Jackson 1999). These microlites of magnetite, with grain sizes in the superparamagnetic (SP) to (SD) size-range, form as high temperature precipitates along the rims of glass shards and within vesicle walls of pumice fragments during high-temperature, vapor-phase crystallization. They are principally composed of acicular or lath shaped crystals that commonly have a strong shape and distribution anisotropy. During fabric development, as the glass shards flow, the microlites have been shown to mimic the fabric created by the shards (Pioli et al. 2008). Therefore, although the microcrystalline Fe-oxides can be either primary or post-

depositional, the orientation and shape of the resultant AMS fabric will largely reflect the flow fabric of the ignimbrite.

Processes controlling fabric formation

This is the first study to systematically sample a continuous vertical section through a large-volume (~ 1 km thick), single ignimbrite cooling unit. Previous studies have shown that welded ignimbrites typically exhibit a planar, oblate fabric, inferred to have formed largely as a result of welding compaction (Ellwood 1982; MacDonald and Palmer 1990; Palmer et al. 1996; Le Pennec et al. 1998; Pioli et al. 2008; LaBerge et al. 2009). Predominately linear, prolate fabrics are not reported as commonly and are typically associated with high-grade rheomorphic ignimbrites (Ellwood 1982; Knight et al. 1986; Pioli et al. 2008). Reports of ignimbrites displaying both oblate and prolate fabrics are even less common (Knight et al. 1986; Pioli et al. 2008; Wilcock et al. 2015). Pioli et al. (2008) examined fabric-shape variation as a function of stratigraphic height in an ~ 8 m section of the rheomorphic Nuraxi Tuff . Willcock et al. (2015) described vertical changes in petrofabric in a ~ 1300 m succession of the non-rheomorphic, intra-caldera Permian Ora ignimbrite in northern Italy. Despite apparent differences in physical conditions and depositional environments, comparison of our analyses to these studies reveals similarities. The ignimbrites are commonly imbricated in the direction of flow and have oblate fabrics toward the base of the sequence, a central interval dominated by linear, prolate fabrics, and an upper oblate layer, suggesting common processes control fabric development in large volume ignimbrites.

Modern concepts of pyroclastic density currents that form ignimbrites are based on field observations, laboratory experiments, and theoretical models. These studies suggest that they comprise stratified flows with a basal dense and concentrated laminar granular fluidized flow region (Fisher et al. 1993; Druitt 1998; Wilson and Walker 1982; Roche et al. 2016) and an overlying dilute turbulent region (Breard and Lube 2017). The concentrated and dilute parts can exchange mass and energy (Doyle et al. 2008; Breard et al. 2017). There is a growing consensus that the massive facies that make up much of volume of ignimbrites are formed by deposition from the concentrated basal granular flowing region. Here, we interpret the magnetic fabrics in the Cardones ignimbrite in terms of deposition from a granular fluidized flow and shear flow during post-emplacement compaction and welding.

In the Cardones, the magnetic foliation (k_3) is aligned ($\alpha_{95} = 6.2°$) and imbricated throughout the entire 1 km cooling unit. This imbrication can be interpreted as a consequence of deposition from the concentrated basal granular flow with an upstream component of accretion (Fig. 13). The ignimbrite is deposited from the basal granular flow as a consequence of loss of pore pressure as the flow advances. We follow Branney and Kokelaar (1992) in envisaging a thin aggradational boundary layer between the flowing granular material and the static deposit. In this interfacial region between flow and deposit, there is pronounced shear.

We propose a waxing and waning history to the basal concentrated flow with a longitudinal and temporal evolution (Fig. 13). The basal flowing region initially grows by transfer of particle mass from the overlying more dilute turbulent regions of the current, perhaps by mechanisms documented in large scale experiments (Breard and Lube 2017). High pore pressures develop in the basal concentrated flow, as envisaged by Roche et al. (2016). As the current propagates, the supply of mass from the overlying current diminishes, the basal

Fig. 13 Schematic representation of the Cardones pyroclastic flow showing a model for the generation of imbrication at three different scales: **a** whole flow including deposit, basal granular flow (BGF), and ash cloud with deposition moving upstream (horizontal scale ~ tens of kms and vertical scale ~ 1 km); **b** velocity profile in the BGF dividing it into a thin (~ 1 m) exponential boundary layer (EBL) and a thicker linear layer; **c** enlargement of box show in panel a in this figure depicting base of the BGF; **d** expansion showing depositional boundary layer region where randomly oriented platy particles become imbricated in the exponential boundary layer
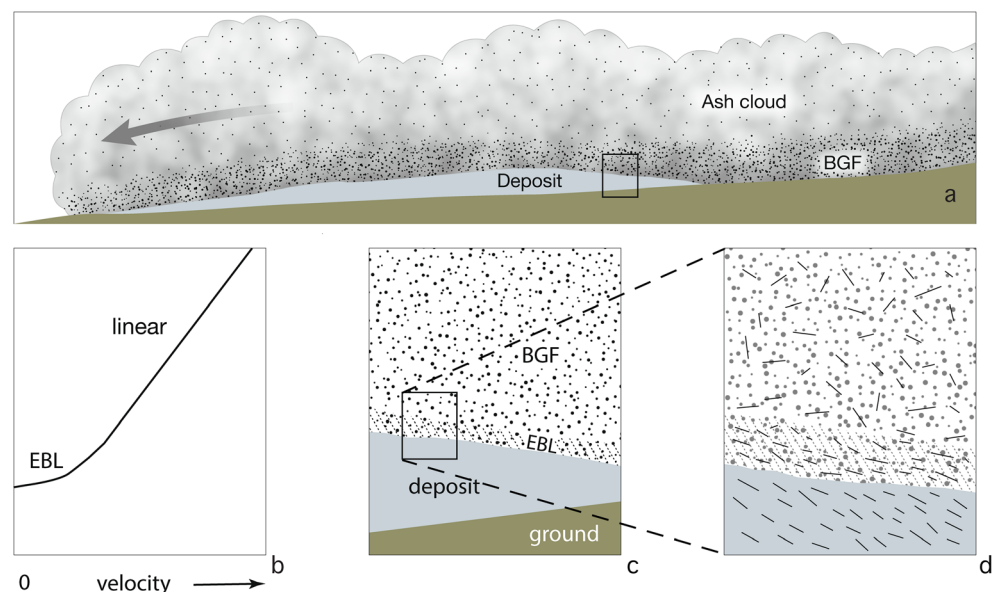
granular region starts to thin, pore pressure dissipates, clast collisions and hence friction coefficient increases, transitioning into a waning and depositional phase (Smith et al. 2018). At the flow front, increasing friction and decreasing pore pressure results in increasing the aggradation rate so the interface between deposited material and shearing material at the flow base slopes upstream. Retrogradational deposition has been documented in analogue granular flow experiments (Smith et al. 2018). Thus the aggradation direction has a vertical and an oblique upstream component. We suggest that imbrication is developed within the boundary layer between the basal concentrated flow and the deposit and is frozen in as the interface moves upwards and upstream. Therefore, it is a combination of three interacting factors: shear in the aggradational boundary layer; stacking up of flat particles at an angle to the depositional surface in the same manner as a cobble acquires an imbrication in a stream; and alignment of particles parallel to the depositional interface, which in retrogradational deposition is oblique to the ultimate base and top of the deposit, which enables elongate particles like glass shards and biotite to develop an initial, syn-depositional imbrication.

The initial syn-depositional fabric is subsequently modified by post-emplacement: loading-compaction and welding; shear; and late tectonic tilting. Modification by post-emplacement gravity-driven, loading-compaction will impose a component of pure shear on the rock volume, flattening the AMS ellipsoid into the bedding plane. Density and fiamme aspect ratio profiles (Fig. 3 and van Zalinge et al. 2016) show that the interior of the Cardones ignimbrite is quite strongly welded. van Zalinge et al. (2016) estimated a maximum 14% decrease of thickness, in the interior of the flow, as a consequence of post-emplacement compaction and deformation. This would flatten the imbrication angle in the central units of the ignimbrite from approximately 25° to the observed mean of 19°. Similarly, post-emplacement flow or late slumping will impose a component of slope-parallel simple shear on the ignimbrite, which will rotate the depositional fabric into the shear plane or superimpose a secondary fabric on the syn-depositional fabric. Finally, late tectonic tilting of ~ 4.5° westward (van Zalinge et al. 2017a) and a hole inclination correction, which the site survey indicates is near vertical (89.6°) at the surface and deviates to $2.9° \pm 0.1°$ toward 249° beginning at ~ 450 m, does not change the fabric shape but it would alter the observed fabric imbrication by approximately 1°.

AMS fabric data reveal that while the orientation of the imbrication remains statistically constant throughout the 1 km thick ignimbrite there is a tendency for it to be slightly flatter and more oblate nearer the margins and somewhat steeper and more prolate in the interior (Fig. 10a). As both post-depositional welding and downslope shear are expected to reduce imbrication angles in the densely welded ignimbrite interior, an attractive explanation for the somewhat higher imbrication angles could be related to lateral changes in

ignimbrite rheology, which thins, cools, and becomes more viscous downslope. A cooler, more viscous flow might produce a damming effect resulting in compression normal to the creep direction and a steepening the imbrication angle during agglutination. Comparable compressional structures are commonly observed in lava flows where the flow front decelerates due to increase in viscosity and more fluid lava piles up behind the flow front (Sparks et al. 1993).

Shape and intensity variation of petrofabric within a stratigraphic succession has been interpreted by previous authors as a combination of changes in welding compaction and simple shear during rheomorphism (Pioli et al. 2008; Knight et al. 1986), increasing shear stress with depth in flow produced by paleotopography, changes in boundary layer conditions or interactions of flow pulses (Branney and Kokelaar 1992; Willcock et al. 2015 An additional alternative is that petrofabric shape and intensity variation in the Cardones ignimbrite might be explained by changes in late-stage strain associated with a depth-dependent variation in emplacement temperatures, cooling rate, and hence viscosity, which allowed late downslope flow and shear in the hot, less viscous interior of the ignimbrite. This flow must have been synchronous with densification by compaction and deformation of the pumice into fiamme.

There is abundant evidence of spatial and temporal temperature variation in the ignimbrite. As the glass transition temperature of hydrous rhyolitic melts (Dingwell 1998; Russell and Quane 2005) similar to the Cardones ignimbrite (van Zalinge et al. 2018) is below 600 °C, uncompacted cuspate and blocky shards (Fig. 3e) observed along the lower margin (~ 940 m), reflect rapid cooling and emplacement temperatures less than 600 °C. After insulation from the substratum, cooler temperatures within the basal unit would likely have persisted as a consequence of the abundant cold lithic clasts included within the basal unit (Marti et al. 1991; van Zalinge et al. 2016). Similarly, within the upper unit (0–180 m), fragmented crystals (Fig. 3b) attest to explosively of eruption (van Zalinge et al. 2018) while spherulites in the glassy material (Fig. 3a) indicate crystallization from temperatures at or near the glass transition (Breitkreuz 2013) and rapid cooling. In contrast, evidence suggests that the interior of the 1 km thick Cardones ignimbrite (Fig. 3c), with fewer lithic clasts and abundant deformed glass shards, was emplaced at temperatures at or above the glass transition and cooled significantly slower. Petrologic data reveal a coincident zone of a low % orthoclase in sanidine (van Zalinge et al. 2016, 2017b) indicating magmatic temperatures ≤ 730 °C in the central units. At these depths, the petrofabrics are likely to have been produced by shear strain imposed on the ignimbrite at temperatures between ~ 500 and 725 °C, where hydrous rhyolite behaves as a fluid (Dingwell 1998; Russell and Quane 2005), yet prior to devitrification of the glass. Modeling results (Riehle et al. 1995) suggest that for rhyolitic glass

significant compaction develops at temperatures above 600 °C for a layer 80 m thick. In addition, for a length scale of 200 m and a thermal diffusivity of 5×10^{-7} m^2/s, the conductive cooling time would be approximately 650 years while the center of the flow (a length scale of 500 m) would have taken of order 10^4 years to cool to temperatures outside the welding window (Russell and Quane 2005). Long residence times at elevated temperatures will enable strain to develop from downslope creep. Under these conditions, the observed prolate, constrictional fabrics, showing downslope elongation, might reflect the basinward narrowing of the deeply incised paleovalley, common in regions with convex hypsometry like the central Andes (Montgomery et al. 2001) or simply downslope creep of a thick flow during compaction.

Conclusions

Rock magnetic results indicate that magnetization of the large-volume Cardones ignimbrite in northern Chile is carried by a mixture of magnetite and hematite/maghemite. These magnetic minerals are both primary and secondary: exsolved within igneous Fe-oxides, along biotite cleavage planes, and in the matrix along rims of glass shards and collapsed voids. The magnetic fabric was thus likely to have been acquired largely post-emplacement mimicking syn-emplacement imbrication of micas and syn and post-emplacement shear of glass shards.

Magnetic fabrics reflect rapid deposition from a concentrated granular fluidized flow with an upstream component of accretion. The ubiquitous imbricated foliation is inclined parallel or sub-parallel to the emplacement direction, indicating flow to the southwest (247°) following a paleo-channel away from its probable source in the Lauca caldera. Systematic vertical sampling through the ~ 1 km-thick cooling unit reveals that the imbrication angle and shape of the magnetic fabric varies systematically with depth in the ignimbrite. The hot-welded interior displays a steeper imbrication and the development of a prolate, predominantly linear fabric while the cooler margins have an oblate, predominately planar fabric and a shallower imbrication. We suggest that superimposed on an inherent temperature variation within the ignimbrite, compression during agglutination and constrictional creep within the narrow, deeply incised paleovalley during rheomorphism might explain both the observed variation in imbrication angle and the development of prolate, linear fabrics. Therefore, measurement of the magnetic petrofabrics in the Cardones ignimbrite allows us not only to constrain the location of the source caldera but yields fundamental insights into depositional and emplacement processes associated with catastrophic, large-volume eruptions.

References

Arason P, Levi S (2010) Maximum likelihood solution for inclination-only data in paleomagnetism. Geophys J Int 182(2):753–771

Baer E, Fisher R, Fuller M, Valentine G (1997) Turbulent transport and deposition of the Ito pyroclastic flow: determinations using anisotropy of magnetic susceptibility. J Geophys Res Solid Earth 102(B10):22565–22586

Bowles JA, Jackson MJ, Berquó TS, Sølheid PA, Gee JS (2013) Inferred time-and temperature-dependent cation ordering in natural titanomagnetites. Nat Commun 4:1916

Brandmeier M, Wörner G (2016) Compositional variations of ignimbrite magmas in the Central Andes over the past 26 Ma—a multivariate statistical perspective. Lithos 262:713–728

Branney MJ, Kokelaar P (1992) A reappraisal of ignimbrite emplacement: progressive aggradation and changes from particulate to non-particulate flow during emplacement of high-grade ignimbrite. Bull Volcanol 54(6):504–520

Branney MJ, Kokelaar PB (2002) Pyroclastic density currents and the sedimentation of ignimbrites. In: Memoir 27. Geological Society, London, p 143

Breard EC, Lube G (2017) Inside pyroclastic density currents–uncovering the enigmatic flow structure and transport behaviour in large-scale experiments. Earth Planet Sci Lett 458:22–36

Breard EC, Dufek J, Lube G (2017) Enhanced mobility in concentrated pyroclastic density currents: an examination of a self-fluidization mechanism. Geophys Res Lett 45(2):654–664

Breitkreuz C (2013) Spherulites and lithophysae—200 years of investigation on high-temperature crystallization domains in silica-rich volcanic rocks. Bull Volcanol 75(4):705

Cande S, Kent D (1995) Revised calibration of the geomagnetic timescale for the Late Cretaceaous and Cenozoic. J Geophys Res Solid Earth 89 100(B4):6095–6095

Cañón-Tapia E, Mendoza-Borunda R (2014) Magnetic petrofabric of igneous rocks: lessons from pyroclastic density current deposits and obsidians. J Volcanol Geotherm Res 289:151–169

Cas RAF, Wright HMN, Folkes CB, Lesti C, Porreca M, Giordano G, Viramonte JG (2011) The flow dynamics of an extremely large volume pyroclastic flow, the 2.08-Ma Cerro Galán ignimbrite, NW Argentina, and comparison with other flow types. Bull Volcanol 73(10):1583–1609

Chadima M, Hrouda F (2009) Cureval 8.0: thermomagnetic curve browser for windows. Agico Inc., Brno

Chadima M, Jelínek V (2008) Anisoft 4.2.–anisotropy data browser. Contrib Geophys Geodesy 38(Special Issue):38–41

Cisowski S (1981) Interacting vs. non-interacting single-domain behavior in natural and synthetic samples. Physic Earth Plan Inter 26:56–62

Dedzo MG, Nédélec A, Nono A, Njanko T, Font E, Kamgang P, Njonfang E, Launeau P (2011) Magnetic fabrics of the Miocene ignimbrites from West-Cameroon: implications for pyroclastic flow source and sedimentation. J Volcanol Geotherm Res 203(3):113–132

Dingwell D (1998) The glass transition in hydrous granitic melts. Phys Earth Planet Inter 107(1–3):1–8

Doyle E, Hogg A, Mader H, Sparks R (2008) Modeling dense pyroclastic basal flows from collapsing columns. Geophys Res Lett 35(4)

Druitt T (1998) Pyroclastic density currents. Geol Soc Lond, Spec Publ 145(1):145–182

Ellwood BB (1982) Estimates of flow direction for calc-alkaline welded tuffs and paleomagnetic data reliability from anisotropy of magnetic susceptibility measurements: Central San Juan Mountains, southwest Colorado. Earth Planet Sci Lett 59(2):303–314

Enkin RJ, Watson GS (1996) Statistical analysis of palaeomagnetic inclination data. Geophys J Int 126(2):495–504

Fisher RV, Orsi G, Ort M, Heiken G (1993) Mobility of a large-volume pyroclastic flow — emplacement of the Campanian ignimbrite, Italy. J Volcanol Geotherm Res 56(3):205–220

García M, Hérail G, Charrier R (1996) The Cenozoic forearc evolution in northern Chile: the western border of the Altiplano of Belén (Chile). In: Third International Symposium of Andean geodynamics, Andean geodynamics. ORSTOM editions. Collection Colloques et Seminaires, Saint Malo, p 362

García M, Gardeweg M, Hérail G, Pérez de Arce C (2000) La ignimbrita Oxaya y la Caldera Lauca: un evento explosivo de gran volumen del Mioceno Inferior en la Región de Arica (Andes Centrales, 18–19 S). In: IX Congreso Geologico Chileno. pp 286–290

García M, Gardeweg M, Clavero J, Hérail G (2004) Arica map: Tarapacá Region, scale 1: 250,000. Carta Geológica de Chile Serie Geología básica 84

García M, Riquelme R, Farías M, Hérail G, Charrier R (2011) Late Miocene–Holocene canyon incision in the western Altiplano, northern Chile: tectonic or climatic forcing? J Geol Soc 168(4):1047–1060

Geissman JW, Newberry NG, Peacor DR (1983) Discrete single-domain and pseudo-single-domain titanomagnetite particles in silicic glass of an ash-flow tuff. Can J Earth Sci 20(2):334–338

Hargraves R, Johnson D, Chan C (1991) Distribution anisotropy: the cause of AMS in igneous rocks? Geophys Res Lett 18(12):2193–2196

Hillhouse JW, Wells RE (1991) Magnetic fabric, flow directions, and source area of the Lower Miocene Peach Springs Tuff in Arizona, California, and Nevada. J Geophys Res Solid Earth (1978–2012) 96(B7):12443–12460

Incoronato A, Addison F, Tarling D, Nardi G, Pescatore T (1983) Magnetic fabric investigations of pyroclastic deposits from Phlegrean fields, southern Italy. Nature 306(5942):461–463

Jackson M, Bowles JA (2014) Curie temperatures of titanomagnetite in ignimbrites: effects of emplacement temperatures, cooling rates, exsolution, and cation ordering. Geochem Geophys Geosyst 15(11):4343–4368

Jelinek V (1981) Characterization of the magnetic fabric of rocks. Tectonophysics 79(3–4):T63–T67

Johnson H, Lowrie W, Kent DV (1975) Stability of anhysteretic remanent magnetization in fine and coarse magnetite and maghemite particles. Geophys J R Astron Soc 41(1):1–10

Jordan TE, Isacks BL, Allmendinger RW, Brewer JA, Ramos VA, Ando CJ (1983) Andean tectonics related to geometry of subducted Nazca plate. Geol Soc Am Bull 94(3):341–361

Knight MD, Walker GP, Ellwood BB, Diehl JF (1986) Stratigraphy, paleomagnetism, and magnetic fabric of the Toba tuffs: constraints on the sources and eruptive styles. J Geophys Res Solid Earth 91(B10):10355–10382

LaBerge RD, Porreca M, Mattei M, Giordano G, Cas RA (2009) Meandering flow of a pyroclastic density current documented by the anisotropy of magnetic susceptibility (AMS) in the quartz latite ignimbrite of the Pleistocene Monte Cimino volcanic centre (central Italy). Tectonophysics 466(1):64–78

Lamarche G, Froggatt PC (1993) New eruptive vents for the Whakamaru ignimbrite (Taupo volcanic zone) identified from magnetic fabric study. N Z J Geol Geophys 36(2):213–222

Le Pennec J-L, Chen Y, Diot H, Froger J-L, Gourgaud A (1998) Interpretation of anisotropy of magnetic susceptibility fabric of ignimbrites in terms of kinematic and sedimentological mechanisms: an Anatolian case-study. Earth Planet Sci Lett 157(1–2):105–127

Lowrie W (1990) Identification of ferromagnetic minerals in a rock by coercivity and unblocking temperature properties. Geophys Res Lett 17(2):159–162

Lowrie W, Fuller M (1971) On the AF demagnetization characteristics of multidomain TRM in magnetite. J Geophys Res Solid Earth 76:6339–6349

MacDonald WD, Palmer HC (1990) Flow directions in ash-flow tuffs: a comparison of geological and magnetic susceptibility measurements, Tshirege member (upper Bandelier Tuff), Valles caldera, New Mexico, USA. Bull Volcanol 53(1):45–59

Marti J, Diez-Gil J, Ortiz R (1991) Conduction model for the thermal influence of lithic clasts in mixtures of hot gases and ejecta. J Geophys Res Solid Earth 96(B13):21879–21885

Martín-Hernández F, Luneburg C, Aubourg M, Jackson M (2004) Magnetic fabric: methods and applications: Geol Soc London Spec

Martinod J, Husson L, Roperch P, Guillaume B, Espurt N (2010) Horizontal subduction zones, convergence velocity and the building of the Andes. Earth Planet Sci Lett 299(3–4):299–309

Mason BG, Pyle DM, Oppenheimer C (2004) The size and frequency of the largest explosive eruptions on earth. Bull Volcanol 66(8):735–748

McFadden P, Reid A (1982) Analysis of palaeomagnetic inclination data. Geophys J R Astron Soc 69(2):307–319

Montgomery DR, Balco G, Willett SD (2001) Climate, tectonics, and the morphology of the Andes. Geology 29(7):579–582

Ort MH (1993) Eruptive processes and caldera formation in a nested downsagcollapse caldera: Cerro Panizos, Central Andes Mountains. J Volcanol Geotherm Res 56(3):221–252

Ort MH, Orsi G, Pappalardo L, Fisher RV (2003) Anisotropy of magnetic susceptibility studies of depositional processes in the Campanian ignimbrite, Italy. Bull Volcanol 65(1):55–72

Ort MH, Newkirk TT, Vilas JF, Vazquez JA (2015) Towards the definition of AMS facies in the deposits of pyroclastic density currents. Geol Soc Lond, Spec Publ 396(1):205–226

Palmer H, MacDonald W, Gromme C, Ellwood B (1996) Magnetic properties and emplacement of the Bishop tuff, California. Bull Volcanol 58(2):101–116

Palmer HC, MacDonald WD (1999) Anisotropy of magnetic susceptibility in relation to source vents of ignimbrites: empirical observations. Tectonophysics 307(1-2):207–218

Pioli L, Lanza R, Ort M, Rosi M (2008) Magnetic fabric, welding texture and strain fabric in the Nuraxi Tuff, Sardinia, Italy. Bull Volcanol 70(9):1123–1137

Porreca M, Mattei M, Giordano G, De Rita D, Funiciello R (2003) Magnetic fabric and implications for pyroclastic flow and lahar emplacement, Albano maar, Italy. J Geophys Res Solid Earth 108(B5)

Ragan D, Sheridan M (1972) Compaction of the Bishop tuff, California. Geol Soc Am Bull 83(1):95–106

Riehle J, Miller T, Bailey R (1995) Cooling, degassing and compaction of rhyolitic ash flow tuffs: a computational model. Bull Volcanol 57(5):319–336

Roche O, Buesch DC, Valentine GA (2016) Slow-moving and far-travelled dense pyroclastic flows during the peach spring super-eruption. Nat Commun 7:10890

Russell JK, Quane SL (2005) Rheology of welding: inversion of field constraints. J Volcanol Geotherm Res 142(1–2):173–191

Saito T, Ishikawa N, Kamata H (2004) Iron–titanium oxide minerals in block-and-ash-flow deposits: implications for lava dome oxidation processes. J Volcanol Geotherm Res 138(3–4):283–294

Salas R, Kast R, Montecinos F, Salas I (1966) Geologia y Recursos Minerales del Departamento de Arica , Provincia de Tarapaca. Inst. de Invest. Geol. Boletin 21:130 p

Scheuber E, Gonzalez G (1999) Tectonics of the Jurassic-early cretaceous magmatic arc of the north Chilean Coastal Cordillera (22°–26° S): a story of crustal deformation along a convergent plate boundary. Tectonics 18(5):895–910

Schlinger CM, Rosenbaum J, Veblen DR (1988) Fe-oxide microcrystals in welded tuff from southern Nevada: origin of remanence carriers by precipitation in volcanic glass. Geology 16(6):556–559

Schröder W, Wörner G (1996) Widespread Cenozoic ignimbrites in N-Chile, W-Bolivia and S-Peru (17°-20°S/71°-68°E): stratigraphy, extension, correlation and origin. In: Third international symposium on Andean geodynamics. Inst. Fr. de Rec. Sci. pour le Dev. en Coop, pp 645–648

Seaman SJ, McIntosh WC, Geissman JW, Williams ML, Elston WE (1991) Magnetic fabrics of the Bloodgood Canyon and Shelley peak tuffs, southwestern New Mexico: implications for emplacement and alteration processes. Bull Volcanol 53(6):460–476

Sheridan MF, Ragan DM (1975) Compaction of ash-flow tuffs. In: Chilingarian GV, Wolf KH (eds) Compaction of coarse-grained sediments. Elsevier, Amsterdam, pp 677–707

Sheridan MF, Wang Y (2005) Cooling and welding history of the Bishop Tuff in Adobe Valley and Chidago canyon, California. J Volcanol Geotherm Res 142(1–2):119–144

Smith RL (1960) Zones and zonal variations in welded ash flows. In: U.S. Geol. Surv. Prof. Pap. pp 149–159

Smith GM, Williams R, Rowley PJ, Parsons DR (2018) Investigation of variable aeration of monodisperse mixtures: implications for pyroclastic density currents. Bull Volcanol 80(8):67

Sparks R, Stasiuk M, Gardeweg M, Swanson D (1993) Welded breccias in andesite lavas. J Geol Soc 150(5):897–902

Sparks R, Tait S, Yanev Y (1999) Dense welding caused by volatile resorption. J Geol Soc 156(2):217–225

Tarling D, Hrouda F (1993) Magnetic anisotropy of rocks. Chapman & Hall, London

Thomas I, Moyer T, Wikswo J Jr (1992) High resolution magnetic susceptibility imaging of geological thin sections: pilot study of a pyroclastic sample from the Bishop Tuff, California, USA. Geophys Res Lett 19(21):2139–2142

Tobar B, Salas I (2015) Cuadrángulos Camaraca y Azapa, Provincia de Tarapacá. Escala 1:50.000

Tosdal RM, Farrar E, Clark AH (1981) K-Ar geochronology of the late Cenozoic volcanic rocks of the cordillera occidental, southernmost Peru. J Volcanol Geotherm Res 10(1–3):157–173

Turner MB, Cronin SJ, Stewart RB, Bebbington M, Smith IE (2008) Using titanomagnetite textures to elucidate volcanic eruption histories. Geology 36(1):31–34

van Zalinge M, Sparks R, Cooper F, Condon D (2016) Early Miocene large-volume ignimbrites of the Oxaya formation, Central Andes. J Geol Soc 173(5):716–733

van Zalinge M, Sparks R, Evenstar L, Cooper F, Aslin J, Condon D (2017a) Using ignimbrites to quantify structural relief growth and understand deformation processes: implications for the development of the Western Andean slope, northernmost Chile. Lithosphere 9(1):29–45

van Zalinge ME, Sparks RSJ, Blundy JD (2017b) Petrogenesis of the large-volume Cardones ignimbrite, Chile; development and destabilization of a complex magma–mush system. J Petrol 58(10):1975–2006

van Zalinge M, Cashman K, Sparks R (2018) Causes of fragmented crystals in ignimbrites: a case study of the Cardones ignimbrite, northern Chile. Bull Volcanol 80(3):22

Vogel, S., Vila, T. (1980) Cuadrangulos Arica y Poconchile. Region e Tarapaca. 1 Mapa Geologico 1: 100.000

Willcock MA, Mattei M, Hasalová P, Giordano G, Cas RA, Morelli C (2015) Flow behaviour in the intra-caldera setting: an AMS study of the large (> 1290 km^3) Permian Ora ignimbrite. Geol Soc Lond Spec Publ 396(1):177–204

Wilson C, Walker GP (1982) Ignimbrite depositional facies: the anatomy of a pyroclastic flow. J Geol Soc 139(5):581–592

Wolff JA, Ellwood BB, Sachs SD (1989) Anisotropy of magnetic susceptibility in welded tuffs: application to a welded-tuff dyke in the Tertiary Trans-Pecos Texas volcanic province, USA. Bull Volcanol 51(4):299–310

Worm HU, Jackson M (1999) The superparamagnetism of Yucca Mountain tuff. J Geophys Res Solid Earth 104(B11):25415–25425

Wörner G, Hammerschmidt K, Henjes-Kunst F, Lezaun J, Wilke H (2000) Geochronology (40Ar/39Ar, K-Ar and He-exposure ages) of Cenozoic magmatic rocks from northern Chile (18-22 S): implications for magmatism and tectonic evolution of the central Andes. Rev Geol Chile 27(2):205–240

Wörner G, Uhlig D, Kohler I, Seyfried H (2002) Evolution of the west Andean escarpment at 18 S (N. Chile) during the last 25 Ma: uplift, erosion and collapse through time. Tectonophysics 345(1–4):183–198